DOE/BC/15311-7
(OSTI ID: 783118)

# VISUALIZATION OF SOLUTION GAS DRIVE IN VISCOUS OIL

SUPRI TR-126
July 2001

By:
D.S. George
A. R. Kovscek

Date Published: July 2001

Work Performed Under Contract No. DE-FC26-00BC15311

Stanford University
Stanford, California

**National Energy Technology Laboratory**
**National Petroleum Technology Office**
**U.S. DEPARTMENT OF ENERGY**
**Tulsa, Oklahoma**

DOE/BC/15311-7
Distribution Category UC-122

# Visualization of Solution Gas Drive in Viscous Oil

By
D.S. George
A.R. Kovscek

July 2001

Work Performed Under Contract DE-FC26-00BC15311

Prepared for
U.S. Department of Energy
Assistant Secretary for Fossil Energy

Thomas Reid, Project Manager
National Petroleum Technology Office
P.O. Box 3628
Tulsa, OK 74101

Prepared by
Stanford University
Department of Petroleum Engineering
Green Earth Sciences Bldg., Room 080b
367 Panama Street
Stanford, CA 94305-2220

## TABLE OF CONTENTS

## LIST OF FIGURES

## ACKNOWLEDGEMENTS

This paper was prepared with the support of the U.S. Department of Energy, under Award No. DE-FC26-00BC15311. However, any opinions, findings, conclusions, or recommendations expressed herein are those of the authors and do not necessarily reflect the views of DOE. Additionally, the support of the SUPRI-A Industrial Affiliates is gratefully acknowledged.

## ABSTRACT

Several experimental studies of solution gas drive are available in the literature, but almost all of the studies have used light oil. Solution gas drive behavior, especially in heavy oil reservoirs, is poorly understood. Hence, experiments were performed in which pore-scale solution gas drive phenomena were viewed in water/carbon dioxide and viscous oil/carbon dioxide systems. A new pressure vessel was designed and constructed to house silicon-wafer micromodels that previously operated at low (< 3 atm) pressure. The new apparatus is used for the visual studies. Several interesting phenomena were viewed. The repeated nucleation of gas bubbles was observed at a gas-wet site occupied by dirt. Interestingly, the dissolution of a gas bubble into the liquid phase was previously recorded at the same nucleation site. Gas bubbles in both systems grew to span one or more pore bodies before mobilization. Liquid viscosity affected the ease with which gas bubbles coalesced. More viscous solutions result in slower rates of coalescence. The transport of solid particles on gas-liquid interfaces was also observed.

# 1. INTRODUCTION

Most solution gas drive experiments have been performed using light oils. Furthermore, only Bora, *et al.* (1997) have performed a micromodel visualization study using heavy oil. There is clearly a need for solution gas drive experimentation to delineate bubble growth and oil production mechanisms using more viscous oils. Silicon-wafer micromodels of the type described by Hornbrook, *et al.* (1991) are used in this study to observe solution gas drive phenomena at the pore scale in water and in viscous oil.

An apparatus was designed to allow the use of silicon-wafer micromodels over a wide range of pressures, as required for solution gas drive experiments. Specifically, a pressure vessel was fabricated to apply the necessary confining pressure to the micromodel. A system of valves and tubing was constructed to provide pressure control for the system. A syringe pump allowed for constant volume expansion rates during pressure decline experiments. Observations of the porous medium were made through a sapphire window using a high-power (200X) microscope.

Expected pore-level flow phenomena, such as snap-off, were successfully observed. Visual observations of gas bubble formation and evolution at a nucleation site were recorded. Experimental results indicated that oil-phase viscosity affects the rate at which pressure changes during pressure decline. Viscosity was also found to affect possibly the ability of gas bubbles to coalesce.

A review of solution gas drive experimentation and theory is presented, followed by a description of the development of micromodels. There is also a discussion of the use of micromodels at high pressure.

## 1.1 Solution Gas Drive

Research on solution gas drive is varied and spans roughly fifty years. Presented here is the research that is most relevant to the effort to observe and explain the mechanism of solution gas drive in porous media.

A solution gas drive reservoir is one in which most of the production is due to the expansion of oil and the originally dissolved gas phase. When the oil is undersaturated, the gas phase does not exist. When reservoir pressure is below the bubble point pressure the oil is saturated. Gas bubbles form, or nucleate, at the bubble point pressure and expand with continued

decreasing pressure. The critical gas saturation ($S_{gc}$) is the percentage of pore space that must be occupied by the gas phase before the gas phase is mobilized.

Many solution gas drive laboratory studies have been performed in which gas bubbles do not nucleate in the liquid when the pressure has dropped below the bubble point. A liquid is supersaturated in such a case. The amount of gas in solution exceeds the equilibrium value for the particular pressure. The critical supersaturation equals $p_e - p_{crit}$, where $p_e$ is the liquid-vapor equilibrium pressure at the initial liquid composition and temperature, and $p_{crit}$ is the liquid pressure at which nucleation first occurs. Few solution gas drive studies have been performed using heavy oils. Most of the literature cited below describes work with light oil.

Kennedy and Olson (1956) used a window cell to observe the formation of bubbles in a mixture of kerosene and methane in the presence of silica and calcite crystals. The time before the first nucleation event was short for high degrees of supersaturation, and was lengthened with decreasing supersaturation. For supersaturations of 30 psi or less nucleation did not occur. Thus, for higher pressure decline rates, greater numbers of bubbles formed. The number of bubbles formed was also observed to depend on the gas diffusion rate through the oil. Bubbles formed on the surface of the silica and calcite crystals.

Stewart, *et al.* (1953, 1956) performed pressure depletion tests using limestone cores to recover a $C_1/C_{10}$-$C_{12}$ mixture by solution gas drive. They estimated the number of bubbles formed for various decline rates, and determined that greater pressure decline rates result in greater numbers of bubbles.

Wood (1953) repeated the experiment performed by Kennedy and Olson (1956) using oil and rock from the Rangely field and found that for a supersaturation of 27 psi no gas bubbles nucleate in agreement with previous work.

Wieland and Kennedy (1957) determined the bubble frequency in cores that underwent pressure decline in a steel bomb. A mixture of East Texas crude oil and methane was used in the experiments. The study showed that greater pressure decline rates result in greater numbers of bubbles, and that low supersaturations (about 25 psi and lower) could be maintained without the occurrence of bubble nucleation. The authors concluded that the properties intrinsic to different types of reservoir rock affected the bubble frequency. They hypothesized that this could be due to the differences in grain surface areas of the different types of reservoir rock and the differences in the surface tensions of the oils used.

Hunt and Berry (1956) applied models for gas-phase growth in bulk liquids to a study of gas-phase growth in porous media. Handy (1958) observed supersaturations of over 200 psi in methane/kerosene mixtures and mixtures of highly refined white oil and methane during solution gas drive tests using low permeability sandstone cores.

Chatenever, *et al.* (1959) made the first microscopic observations of solution gas drive behavior, using a butane-saturated mineral oil in glass bead packs and thin sections of sandstone and limestone. They observed that capillary forces significantly affected bubble growth, and concluded that the displacement of oil in a solution gas drive is caused by existing microscopic gas structures instead of by the formation of new gas bubbles. They also observed that after a gas bubble was formed, it coalesced with other gas structures, eventually forming a long, narrow, continuous gas bubble.

Dumore (1970) performed solution gas drive experiments in transparent models filled with glass beads, using a $C_1$/kerosene/novasol mixture. According to the data, the maximum supersaturation occurred after the occurrence of nucleation. It was concluded that $S_{gc}$ depends on capillary effects.

Visual studies performed by Wall and Khurana (1971, 1972) indicated that nucleation in porous media begins in supersaturated liquid. High pressure decline rates were observed to lead to high degrees of supersaturation. Gas bubbles were observed to grow and coalesce after nucleation.

Abgrall and Iffly (1973) measured $S_{gc}$ using reservoir crude oil in vuggy and intergranular rock. They developed a model that predicts the supersaturation necessary for the occurrence of nucleation. In the model this critical supersaturation is not dependent on the pressure decline rate. One experiment performed by Madaoui (1975) indicated that $S_{gc}$ was nearly unrelated to the pressure decline rate.

Danesh, *et al.* (1987) performed solution gas drive experiments on North Sea separator crude oils recombined with a nine-component gas mixture. A high-pressure etched-glass micromodel was used. The pressure had to be lowered below the bubble point for nucleation to occur. Supersaturations ranged from 30 psi to 770 psi. The first bubbles to nucleate appeared in pore bodies or wide channels. Actual nucleation events, however, could not be observed. After nucleation, bubbles grew by diffusion. They were eventually mobilized and moved by jumps.

Snap-off of the long gas bubbles was also observed. Moulu and Longeron (1989) reported for a C1/C3/C10 mixture that the pressure decline rate affected the degree of supersaturation and $S_{gc}$.

Yortsos and Parlar (1989) conducted a study of gas formation in porous media. They made a distinction between nucleation processes and gas-phase growth. The nucleation of gas in porous media was modeled as heterogeneous nucleation, a process in which gas bubbles form from specific nucleation sites that contain trapped gas (pre-exisent or nucleated) on pore walls. Nucleation occurs when the local supersaturation pressure becomes greater than the capillary pressure at the site, causing the liberation of a gas bubble. The authors stated that this process occurs at various nucleation sites, all of which are activated as a function of supersaturation. They found that nucleation is most likely to occur in the largest pores first. For the first time, it was stated that nucleation does not depend on the kinetics of homogeneous nucleation or heterogeneous nucleation, but only on the concentration of the volatile species and on the liquid pressure. Furthermore, an analysis of the growth of a single gas bubble after nucleation was performed. A percolation model for gas-phase growth that is valid for low pressure decline rates was developed. The authors determined that for low pressure decline rates, for which capillary forces are dominant, $S_{gc}$ is a function of the nucleation characteristics of the porous medium, which are dependant on pore geometry. For cases in which capillary effects are not dominant, it was suggested that the growth of the gas phase could be modeled by diffusion-limited aggregation (DLA). For DLA-type gas-phase growth, no equilibrium states exist except complete saturation of the porous medium by gas, with the exception of the existence of trapped liquid.

Firoozabadi, *et al.* (1992) performed solution gas drive experiments using a $C_1$/n-$C_{10}$ mixture in Berea sandstone and chalk cores. In some of the experiments, a light mixture of about 35% $C_{10}$ was used. In other experiments a heavier composition of about 70% $C_{10}$ was used. A pump with a fixed expansion rate was used to avoid sudden pressure changes. The authors concluded that, even at high expansion rates, supersaturation in porous media could be negligible. They also found that pore structure could affect the degree of supersaturation such that a rock with smaller grains could display less supersaturation than a rock with larger grains. They stated that $S_{gc}$ is a function of both supersaturation and pore structure.

Kortekaas and van Poelgeest (1991) measured $S_{gc}$ for light, two-component hydrocarbon mixtures in clean, water-wet cores with the presence of connate water. They concluded that

increasing pressure decline rates result in an increase in $S_{gc}$, and that pore structure is important during nucleation.

Li and Yortsos (1991) visualized gas formation by pressure decline in a carbonated water system using a Hele-Shaw cell and a glass micromodel. In the Hele-Shaw cell, nucleation occurred at different sites forming nearly radial bubbles that exhibited compact growth at early stages. Compact growth is the growth of all bubbles simultaneously in rate and size. As the bubbles grew they would frequently coalesce, eventually leading to the formation of a large, dominant bubble. Nucleation was observed to occur at various sites in the micromodel, but growth occurred in a ramified (branching) fashion. The critical gas saturation was found to decrease with increasing pressure decline rates; an observation that conflicted with several results reported in the literature (Firoozabadi, *et al.*, 1992; Kortekaas and van Poelgeest, 1991; Firoozabadi and Kashchiev, 1996). A numerical pore network model was developed to simulate nucleation and growth of the gas phase in porous media. The model accounted for nucleation, gas expansion, mass transfer growth, concentration gradients, and finite size effects. The numerical results were found to approximate the experimental results.

Li and Yortsos (1993) further developed the theoretical analysis and pore network simulation of bubble growth in porous media, this time considering the growth of both single and multiple gas clusters.

Li and Yortsos (1994) studied the stability of a single bubble growing in an effective porous medium with constant supersaturation. A new stabilization mechanism was identified based on convective transport in the growing phase. This stabilization mechanism was found to be strong for high mobility ratios. Experiments using Hele-Shaw cells were performed to support the findings of the study.

Li and Yortsos (1995a) observed the growth of the gas phase in a carbonated water system in etched-glass micromodels and Hele-Shaw cells. They found that the growth of the gas phase in micromodels led to ramified patterns in gas clusters, while the growth of the gas phase in Hele-Shaw cells was much more compact. A pore network simulator was developed that predicted growth patterns of the gas phase in porous media. The simulator showed reasonable agreement with the experimental results. Satik, *et al.* (1995) described scaling behavior for single bubble growth in porous media in three dimensions. The authors determined that for conditions of low supersaturation, the rate of growth scales as $t^{1/(D_f-1)}$, where $D_f$ is the pattern fractal

dimension. They found $D_f$ to equal 2.5 for bubble growth in three-dimensional porous media. Hence, instead of the classical $t^{1/2}$ scaling for diffusional growth they found $t^{2/3}$. The scaling behavior described by the authors predicts a faster bubble growth rate compared to classical scaling behavior.

Li and Yortsos (1995b) performed a systematic theoretical analysis of bubble growth in porous media, with a strong emphasis on modeling $S_{gc}$. Three different regimes of gas-phase growth behavior were identified for the growth of multiple gas clusters. For cases in which the pressure decline rate is sufficiently low, such that growth is completely controlled by capillarity, global percolation was identified as the growth mechanism. During growth by global percolation the largest throat fills with gas, without regard to the size or location of the gas cluster of which it becomes a part. For higher pressure decline rates a combination of percolation rules governing the advance of each gas cluster and DLA rules governing the mass transfer was used to model the growth of the gas phase. This growth regime is called "percolation-DLA." A third regime, "percolation-modified-DLA," was also identified. The critical gas saturation was found to be completely dependent on the nucleation fraction when growth is controlled by global percolation. Furthermore, $S_{gc}$ was also found to be independent of the pressure decline rate in cases for which the pressure decline rate was high. The authors theorized that a larger nucleation fraction, caused by a higher pressure decline rate, is what causes an increase in $S_{gc}$. The authors stated that solution gas drive results depend on the underlying growth pattern of gas clusters.

Firoozabadi and Kashchiev (1996) developed a simple model to describe gas-phase growth in porous media that challenged the classical theory of heterogeneous nucleation. They claimed that their experiments, along with experimental results found in the literature, support an instantaneous nucleation model instead of a heterogeneous nucleation model. The instantaneous nucleation model was derived from theories related to the growth of the gas phase in bulk liquids. According to the authors, nucleation at all sites occurs at the same instant, and supersaturation is affected by the pressure decline rate.

Yortsos (1997) defended the heterogeneous nucleation model, arguing that the results of his work are consistent with experimental results and that instantaneous nucleation was not observed in his experimental work. He argued that Firoozabadi and Kashchiev (1996) modeled the critical gas saturation using theory that was developed for the growth of a single isolated bubble in a bulk fluid, as opposed to multiple bubbles in a porous medium.

Firoozabadi (1997) in turn questioned the experimental methods of Li and Yortsos, and he reiterated his opinion that critical supersaturation is not the supersaturation pressure needed to activate an individual nucleation site on a pore wall by overcoming capillary pressure. He also disagreed with the model of $S_{gc}$ proposed by Li and Yortsos, asserting that it is based on constant bubble density and is independent of rate.

El-Yousfi, *et al.* (1997) studied the liberation of $CO_2$ from supersaturated carbonated water in resin and glass micromodels. They concluded that neither heterogeneous nucleation nor instantaneous nucleation could explain their results. To explain the results a new model of capillary trapping was developed, by which drawdown balances capillary trapping, resulting in the activation of a nucleation site. The authors determined that instantaneous nucleation was not a satisfactory explanation of what happens at the pore scale during nucleation, but that it provides a suitable approximation of the experimental results. Unfortunately, bubbles could not be observed until they grew to a size of 30 μm, well after the corresponding nucleation sites were activated. The authors also noted the tendency for the gas phase to develop ramified patterns.

Bora, *et al.* (1997) conducted a high-pressure micromodel study of solution gas drive behavior in heavy oil. Five different natural and synthetic oils were used, one of which was Lindbergh heavy crude oil. Their experiments were not true depletion experiments. They maintained a supply of crude oil to the micromodel at fixed pressure. They observed that the presence of asphaltenes tended to hinder bubble coalescence, and noted that wettability did not appear to be a critical parameter for solution gas drive processes.

## 1.2 Micromodels

Micromodels are produced with the objective of directly observing fluid flow through porous media. Micromodels contain an etched flow pattern that can be viewed with a microscope. The flow pattern can be a lattice of straight or constricted channels, or the pore network can be modeled after the pores found in naturally occurring rock. A limitation that is inherent to all micromodels is that they are only two-dimensional. Numerous studies have been performed using etched-glass micromodels. Etched-glass micromodels have been made with actual rock pore patterns, but the etching process required pore sizes to be increased to several times larger than actual. Also, the necessary bonding processes resulted in a loss of surface roughness.

Mattax and Kyte (1961) developed the first etched-glass micromodel. The model consisted of a network of straight, interconnected flow channels. The micromodel provided a superior means for viewing interfaces in porous media. It was used to study the effect of wettability on waterflood oil production.

Davis and Jones (1968) applied an etching technique that resulted in the construction of superior micromodels. A photosensitive resist that becomes resistant to many solvents after exposure to ultraviolet light was coated on a glass surface. Any black and white pattern could be projected onto the photosensitive resist, rendering part of the glass impervious to etching. This provided the ability to etch complex patterns in glass, resulting in micromodels with complex pore structures.

Instead of using a glass substrate, Owete and Brigham (1987) developed silicon-wafer micromodels that allowed for increased control of etch depth and more accurate reproduction of fine-scale details. A flow pattern was etched on a silicon wafer, which was then oxidized to produce a water-wet porous medium. The flow area was sealed with a glass plate that was anodically bonded to the silicon wafer.

The micromodels developed by Hornbrook, *et al.* (1991) are superior to etched-glass micromodels. An almost exact replica of a thin section of Berea sandstone is reproduced on a silicon wafer, using a scanning-electron microscope (SEM) image of the thin section. Because the SEM image can only cover a very small area, the pattern on the image was repeated across the etched area of the silicon wafer. These micromodels possess roughness and wettability characteristics that are approximately equal to those of the original sandstone. Furthermore, when the micromodels are produced the depth of the pore and channel network can be controlled with great accuracy.

Since 1985, several micromodel studies have been performed at elevated pressures. The studies focused on a variety of phenomena that are affected by pressure, and various types of pressure vessels have been designed to allow the observation of micromodels at high pressure.

Campbell and Orr (1985) performed a high pressure visualization study of the displacement of crude oil by $CO_2$. An etched-glass micromodel was placed in a pressure vessel, and experiments were performed at pressures of up to 1200 psia.

Peden and Husain (1985) built a pressure vessel that housed etched-glass micromodels and provided a confining pressure of 6000 psi. They used the vessel to visualize multiphase flow

through porous media and $CO_2$ flooding. Danesh, *et al.* (1987) used the vessel described by Peden and Husain (1985) to observe solution gas drive processes at the pore scale.

Kuhlman (1990) designed a high-pressure cell that housed etched-glass micromodels in order to observe interactions between foam and oil. Coşkuner (1997) used a pressure vessel similar to that of Kuhlman (1990) that housed etched-glass micromodels. High pressure experiments were performed to study gas condensate flow in porous media. Bora, *et al.* (1997) used a high-pressure micromodel to observe solution gas drive processes in heavy oil. An etched-glass plate was held against a smooth glass plate by overburden pressure inside a windowed pressure vessel.

Mackay, *et al.* (1998) used the vessel described by Peden and Husain (1985) to study the effect of gas-oil interfacial tension (IFT) on flow behavior. They conducted experiments with etched-glass micromodels at pressures up to 5000 psia. The longest of these high-pressure experiments lasted for 54 days. They found that the gas-oil IFT has a profound effect on the loci and distribution of gas bubbles in porous media. It was found that supersaturation is negligible for systems with low gas-oil IFT. Furthermore, at low pressure-decline rates supersaturation was found to be negligible regardless of the IFT. The IFT was observed to determine whether gas nucleation occurs in the oil phase or in the water phase. IFT also determines capillary pressures that affect the mobility of gas bubbles.

## 2. EXPERIMENTAL APPARATUS

The experimental apparatus for this study consists of the micromodel, pressure vessel, optical equipment, and a system of hardware that controls fluid flow and pressure, as shown in Figure 2.1. Several tests were performed to verify the structural integrity of the apparatus, and to verify the capability to obtain visual data from the micromodel.

### 2.1 Micromodels

Etched-silicon-wafer micromodels of the type developed by Hornbrook *et al.* (1991) were used in this project. The micromodels contain a 5 cm by 5 cm etched pore pattern. There are two etched inlet/outlet ports at opposite corners of the pore network. Holes are drilled into the silicon wafer at these ports, providing locations that allow fluid to enter and exit the micromodel. These

micromodels contain a modification introduced by Castanier and Sagar (1998): narrow etched channels adjacent to the edges of the pore network carry fluid to the inlet/outlet ports as shown in Fig. 2.2. These channels allow fluid to enter and exit the porous medium not just at a corner, but along most of a side of the pore network. The result of the channels is linear flow, as opposed to radial flow, near the inlet and outlet of the micromodel. The porosity of the micromodel is roughly 0.2. The permeability of the micromodel is approximately 0.1 mD.

The etched side of a silicon wafer is anodically bonded to a borosilicate glass plate in order to produce a micromodel. During anodic bonding, the surfaces of the silicon wafer and glass plate are in contact. The silicon wafer is placed on an anode. The glass plate rests on top of the silicon wafer. A cathode is placed on top of the glass plate. Significant effort was placed on a redetermination of the optimum bonding parameters rather than relying on the information of Hornbrook *et al.* (1991). The system is heated to 600 °F and the electrodes are charged to 1000 V after alignment of the micromodel and cover plate on the bonding apparatus. During the bonding process the pore surfaces of the silicon wafer are oxidized because they are in the presence of air at high temperature. The optimum bonding time is one hour, after which the electricity is turned off and the new micromodel is allowed to cool.

## 2.2 Pressure Vessel

The bond that holds an etched-silicon-wafer to a glass cover plate may fail when the difference between internal and external pressure is greater than about 30 psi. In order to achieve the goal of performing solution gas drive experiments in silicon-wafer micromodels at elevated pressures, a vessel in which a micromodel can be housed has been designed and constructed. The pressure vessel has a maximum operating pressure of 1000 psig. The temperature of the vessel can be controlled, ranging from 15°C to 100°C, if the confining fluid is circulated through a temperature-control bath. Because the surface of the silicon-wafer micromodel is oxidized, the use of silicon-wafer micromodels at higher temperatures demands some reconsideration. Silicon dioxide ($SiO_2$) is appreciably soluble in water at elevated temperatures.

The pressure vessel is made of 6061 T6 aluminum. The micromodel sits inside the body of the pressure vessel. Holes that serve as fluid inlet/outlet ports are drilled in the bottom of the micromodel. These holes rest directly above machined channels that carry fluid to and from the micromodel. O-rings are used to create a seal where the tubes meet the inlet/outlet ports of the

micromodel as shown in Fig. 2.3. Confining liquid is used to provide pressure support to the micromodel. If temperature control is not needed, the confining liquid can remain static. The vessel is designed, however, to allow temperature-controlled confining liquid to circulate through the interior of the pressure vessel, entering and exiting through tubes that are located on opposite sides of the vessel. A 0.185 in thick sapphire window is located directly above the micromodel. Sapphire was selected because of its superior mechanical and optical qualities. The window is held between the micromodel and the pressure vessel lid in a manner such that its edges are considered to be fixed (Fig. 2.4). This leads to maximum mechanical strength. An O-ring between the lid and the window seals the space. The pressure vessel lid is shaped like an annular ring. The lid fits over both the body of the pressure vessel and the window, such that the window, and thus the micromodel, is viewed in the center of the annular ring.

In order to prevent failure of the pressure vessel and to protect users, some safety features are implemented. A confining liquid is used because liquid will not expand as much as gas in the event of failure. A modified hydraulic cylinder is used to pressurize the confining liquid without allowing the liquid to contact the pressurizing gas. This prevents the liquid from saturating with gas and increasing liquid compressibility significantly. In order to assure that no gas enters the confining liquid chamber, the pressure vessel is assembled under water. The pressure system was designed for 1500 psi, even though the maximum operating pressure of the system is nominally 1000 psi. Thus, a safety factor of 1.5 was established. The lid, Fig. 2.4, is machined from a solid piece of aluminum. The entire window is not exposed by the lid. Several bars that provide additional support to the sapphire window cover the opening in the center of the vessel lid.

## 2.3 Optics

A microscope (Nikon, Optiphot-M) with a photo tube that allows for the connection of a video camera was used. Because the silicon-wafer micromodels are opaque, a light source inside of the microscope sends light through the objective lens in order to illuminate the micromodel. Light is reflected off the micromodel, providing an image of the porous medium. The image enters the objective lens, and is sent to the ocular lenses and to the photo tube. The ocular lenses of the microscope provide 10X magnification. A high-quality color video camera (PULNiX, TMC-7RGB, Sunnyvale, CA) is connected to the photo tube. Images are sent from the video camera to a VCR for recording. An extra-long working distance objective lens (Nikon,

MPLAN-20 0.4 ELWD) with a 4 mm working distance was used. The thickness of the sapphire window (4.7 mm), combined with the thickness of the micromodel cover glass (1 mm), results in a total cover glass thickness of 5.7 mm. This thickness is greater than the working distance of the objective lens by 1 mm. A loss of image quality, mainly due to a loss in contrast, occurs as a result.

The superior mechanical strength and optical qualities of sapphire provide the advantages of a short working distance and high transmission of light. The fact that sapphire has anisotropic optical properties, however, causes double refraction images that reduce image quality. The image of the micromodel that is transmitted by the objective lens contains "phantom images" that are due to double refraction. The double refraction images are much lighter than the real images. Although the phantom images reduce image quality, the image remains easily interpretable.

## 2.4 Pressure System

Carbon dioxide from a high-pressure cylinder is used to pressurize water. To avoid carbonating the confining water it is pressurized in a modified hydraulic cylinder (Miller Fluid Power, HV50R2N, Bensenville, IL) as shown in Fig. 2.5. A piston in the hydraulic cylinder separates the pressurized gas from the confining water. Because the gas is not in contact with the liquid, the liquid cannot become saturated with the gas. If the liquid were saturated with gas and failure occurred, the loss of pressure would cause gas to come out of solution. This gas would expand rapidly, potentially causing an explosion. If the confining liquid is not in contact with the gas, then no gas will form in the confining liquid in the event of failure preventing the uncontrolled release of pressure. The piston is free to move across the length of the hydraulic cylinder. A pressure gauge indicates the pressure of the confining liquid.

A pressurized $CO_2$ cylinder provides both injection pressure for the micromodel and confining pressure for the vessel. The fluid that is pumped into the micromodel is pressurized by $CO_2$ in a bomb. A three-way valve controls whether oil or $CO_2$ is pumped through the micromodel. A plug valve isolates the micromodel from upstream fluids so that depletion experiments can be conducted. Pressure gauges indicate the pressures upstream and downstream of the micromodel. On the downstream side of the micromodel, a three-way valve is used to select whether the outlet from the micromodel will be connected to a syringe pump (ISCO,

100DM, Linclon, NE), or whether the fluids leaving the micromodel will be allowed to exit the system at atmospheric pressure.

The syringe pump is used to provide back pressure and to control the flow of fluid out of the micromodel. The small micromodel volume of 0.015 mL necessitates the capability to withdraw fluid at very low rates. The syringe pump provides this capability, as it has a minimum refill rate of 0.0001 mL/min.

## 2.5 Tests

After the vessel was produced, it underwent a pressure test. The vessel successfully contained water that was pressurized to 940 psi for one hour. No leaks or structural failures occurred.

Another test was carried out in order to determine whether pore-scale flow events could be observed clearly using the pressure vessel with the optics selected for this study. A 0.1 wt. % AOS 14-16 (alpha olefin sulfonate with a chain length of 14-16 carbons) solution was prepared and used as the surfactant solution for this experiment. A slug of surfactant solution was injected into a dry micromodel, and nitrogen ($N_2$) was then injected into the slug. This experiment was performed at injection pressures lower than 30 psig, so the use of confining liquid was not necessary. The formation of foam was observed, and microscopic events such as snap-off were identified.

A third test was performed in which water was saturated with $N_2$ at about 900 psig. This liquid was allowed to enter the micromodel, after which the pressure was allowed to drop to 0 psig. The point at which bubble nucleation began was not recorded, but gas formation and evolution were successfully observed.

Next, an attempt was made to observe solution gas drive processes in Kaydol, a 220 cp white mineral oil. The experimental procedure was as follows:

1. Kaydol was saturated with $CO_2$ at 520 psig in a bomb for six hours. During this time, the micromodel was swept with $CO_2$ in order to displace air.
2. The flow of $CO_2$ through the micromodel was stopped, and the micromodel was allowed to saturate with the gas-saturated Kaydol.
3. The upstream pressure was increased to 600 psig, and a back pressure of 580 psig was applied.

4. The micromodel was shut in on both sides.
5. The back pressure was decreased, and the pressures upstream and downstream from the micromodel were recorded at various times. The pressure drop across the porous medium, $\Delta p$, was calculated for each measurement.

There were three major differences between the set-up used in this experiment and the set-up described in Section 2.4 of this report. First, the back pressure was controlled by pressurized gas instead of by a syringe pump. The rate of flow from the micromodel could not be controlled with accuracy as a result. The back pressure was not constant with time because a valve was used to isolate the micromodel from the gas cylinder that provided the back pressure. This led to increases in the back pressure after the micromodel was shut in, until pressure equilibrium was reached ($\Delta p = 0$) and flow through the micromodel stopped. When equilibrium was reached, the back-pressure was decreased by releasing $CO_2$ from a needle valve. This occasionally resulted in large, sudden decreases in downstream pressure. This variable downstream pressure was a poorly posed boundary condition. The second major difference between this experiment and future experiments was that the confining water was pressurized by $CO_2$ in a bomb, instead of in the modified hydraulic cylinder described in Section 2.4 of this report. This allowed the confining water, in which $CO_2$ was highly soluble, to become saturated with $CO_2$ at high pressures. Finally, the opening in the vessel lid did not have bars to support the sapphire window.

Throughout the experiment the pressure in the micromodel gradually decreased from an initial pressure of 600 psig. The experiment was halted by a failure of the pressure vessel window when the average pressure in the micromodel was 420 psig. Pressure in the vessel dropped suddenly, leading to rapid liberation and expansion of gas that was previously in solution with the confining water. The sapphire window was destroyed and the micromodel that was housed in the pressure vessel failed due to the loss of confining pressure. Figure 2.6 is a photograph of the window assembled after the failure.

The confining water pressure was 600 psig at the time of the explosion, and the sapphire window had previously withstood significantly higher pressures. Furthermore, the sapphire window was designed to withstand 1500 psig. An inspection of the pressure vessel lid revealed some burrs in the area contacted by the window that could have point-loaded the sapphire window and caused damage.

A second attempt was made to observe solution gas drive processes in $CO_2$-saturated Kaydol. A new sapphire window was used, and the modified hydraulic cylinder was used to prevent gas from entering solution with the confining water. The new window failed at 580 psig during the initial pressurization of the vessel. Because the window was new it is unlikely that it was damaged before or during use. The cause of failure was not successfully determined. Based on the observation that both window failures occurred at around 600 psig, it was decided that experimentation would continue, with the use of a sapphire window, but at a maximum pressure of 300 psig. Bars were added to the vessel lid, as mentioned in Section 2.2, in order to provide additional support to the sapphire window.

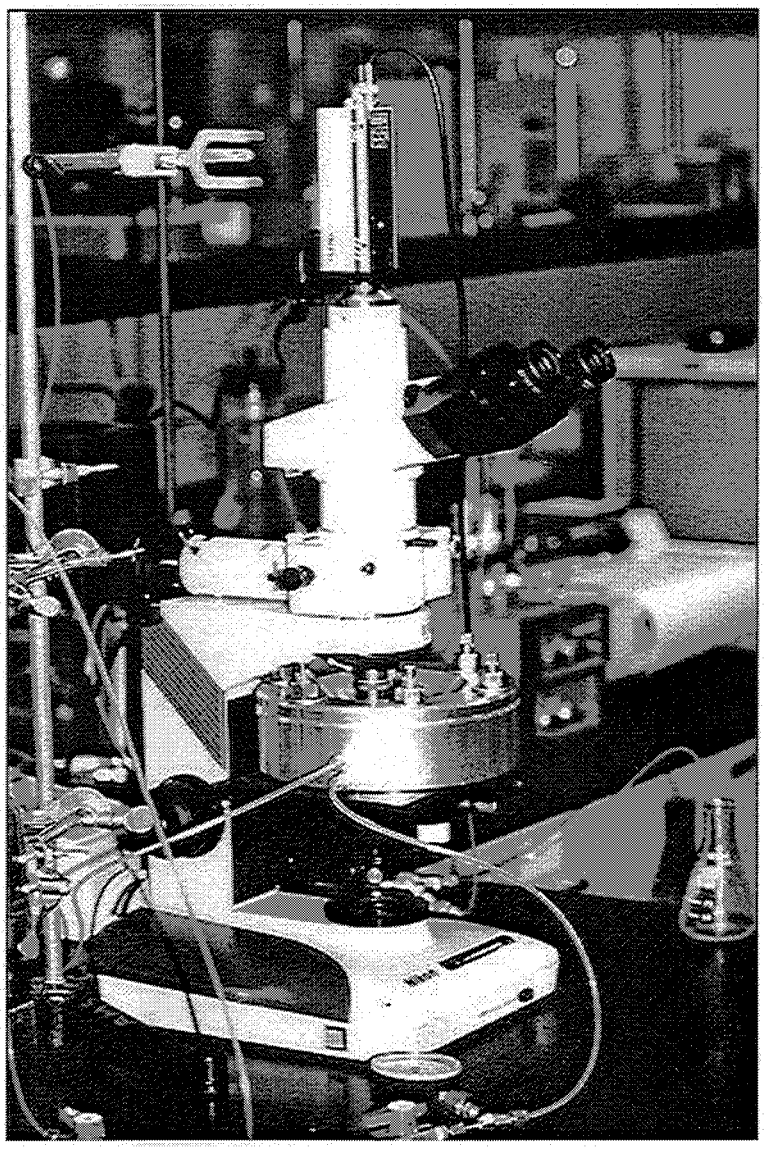

**Figure 2.1: The video camera, microscope, and pressure vessel.**

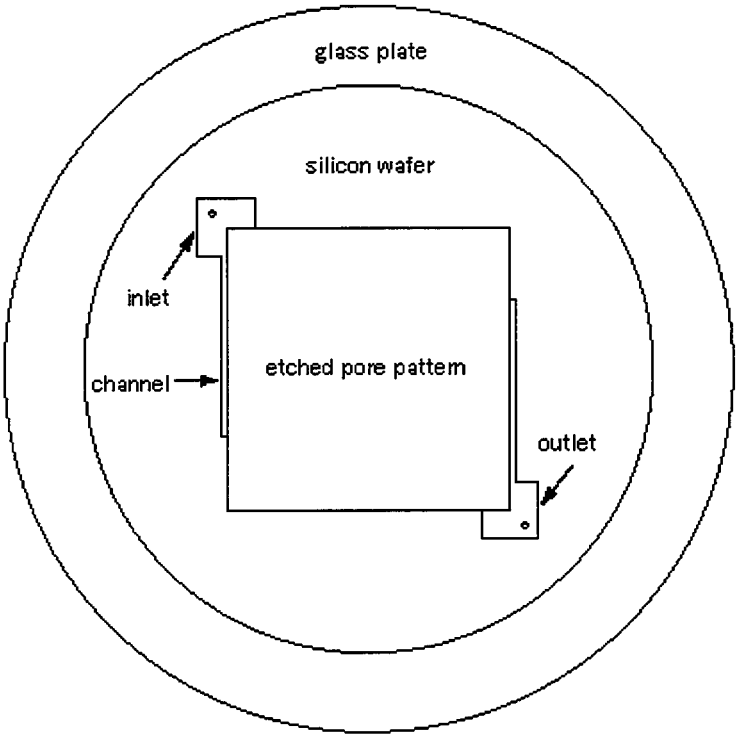


**Figure 2.2: Schematic of the silicon-wafer micromodel.**

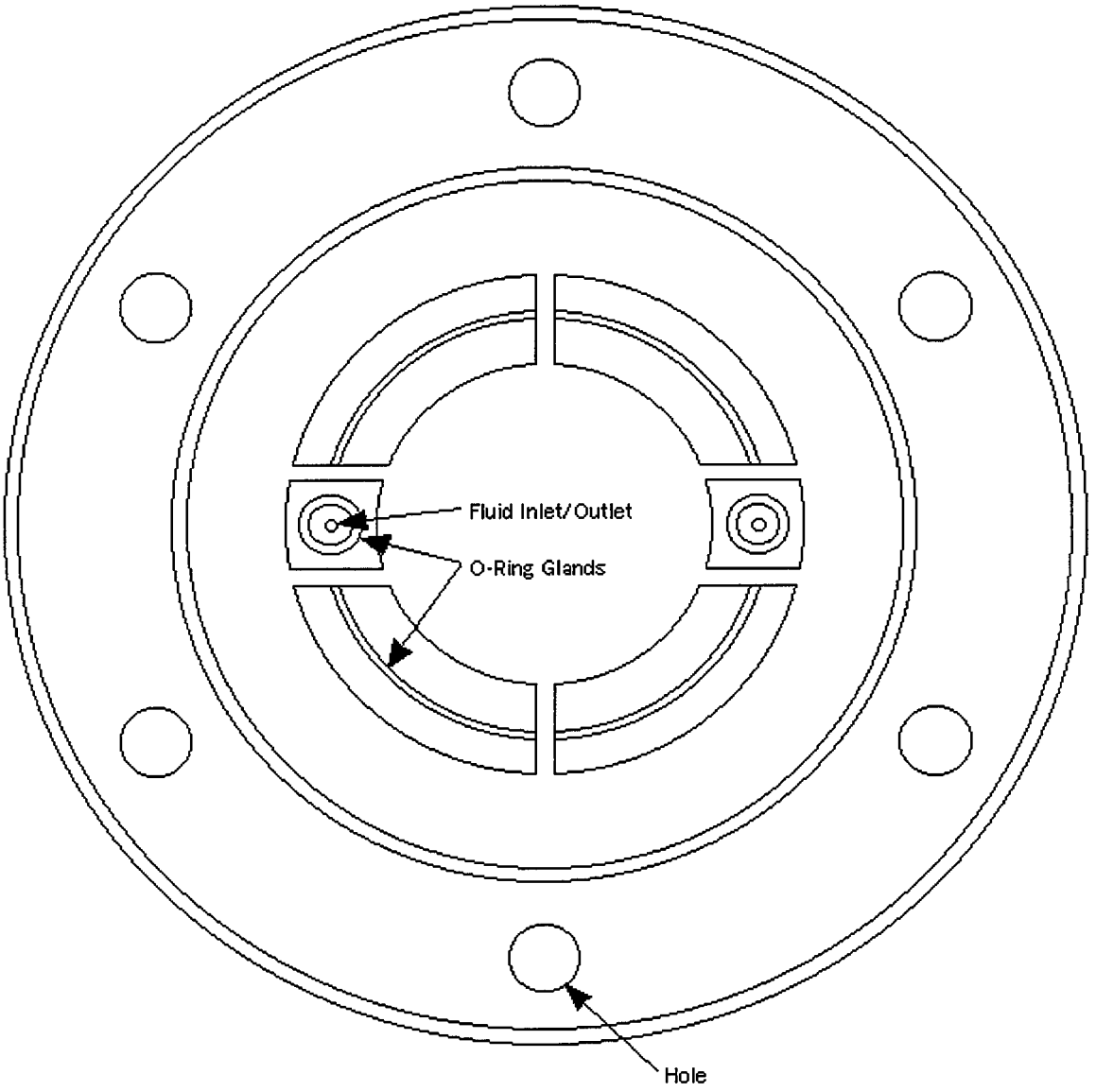


**Figure 2.3: Plan view of the pressure vessel.**

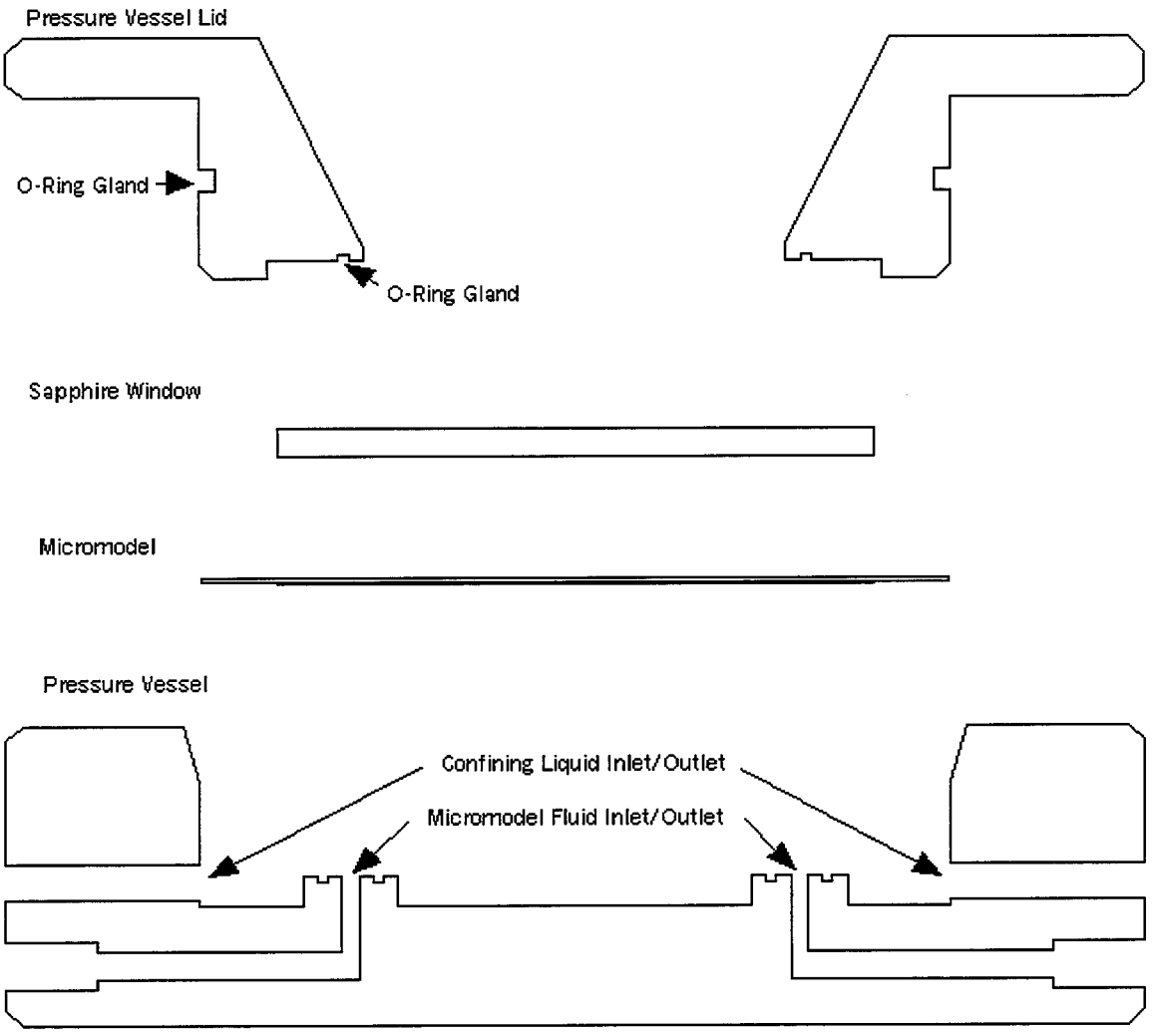


**Figure 2.4: Exploded view of the pressure vessel components.**

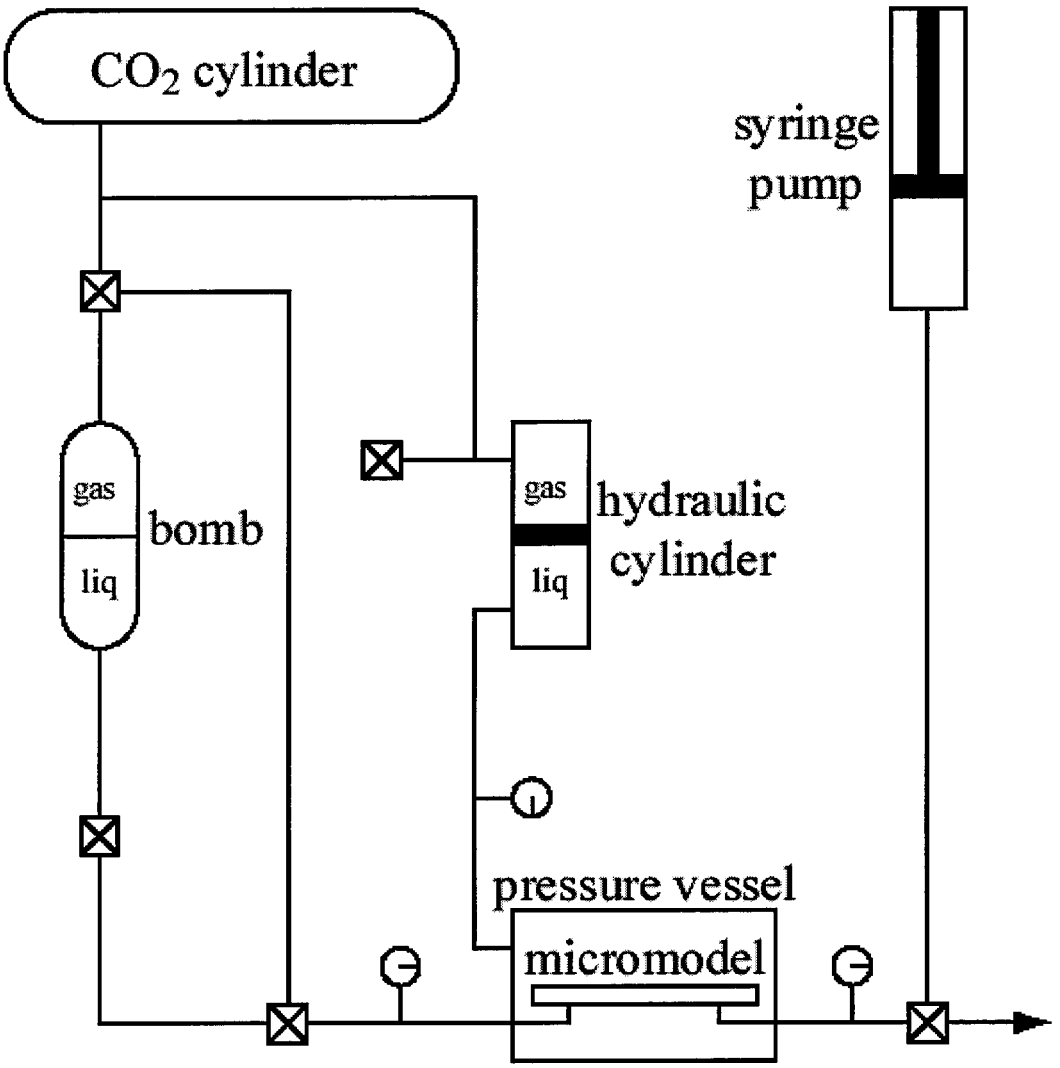


**Figure 2.5: Schematic of the pressure system.**

**Figure 2.6: Sapphire window assembled after failure.**

# 3. RESULTS

Solution gas drive experiments were performed using $CO_2$-saturated water and later $CO_2$-saturated Kaydol. An attempt was made to follow these general guidelines:

1. The liquid was saturated with $CO_2$ at the desired pressure for a minimum of 20 hours.
2. If the micromodel contained air, $CO_2$ was injected and allowed to sweep the micromodel to displace the air.
3. The upstream pressure was increased to the desired injection pressure, and the injection of live liquid was initiated.
4. Sufficient time was allotted for the micromodel to saturate with the liquid, and for some fluid to exit the micromodel.
5. The three-way valve on the downstream side of the pressure vessel was turned such that the outlet of the micromodel was connected to the syringe pump. The pump was then run until the outlet pressure reached the inlet pressure.
6. The valve on the upstream side of the pressure vessel was shut. At this point the volume between the valve and the syringe pump, including the porous medium, pressure gauges, and tubing, was closed.
7. Once the inlet and outlet pressures equilibrated ($\Delta p = 0$), the syringe pump refilled at a low flow rate, providing a controlled volume expansion.
8. The upstream and downstream pressures were recorded against time, and the VCR recorded pore-level visual observations.

There is a large amount of dead space (tubing, pressure gauges, etc.) within the controlled volume relative to the volume of the micromodel. Even with the length of tubing kept to a minimum, the volume of dead space was approximately 25 mL, while the volume of the porous medium was 0.015 mL. This is an undesirable but common aspect of micromodel experiments.

Next, a series of experiments are summarized and discussed. Water and $CO_2$ results are shown first, and then Kaydol and $CO_2$ work follows.

## 3.1 Water Saturated with $CO_2$ at 100 psig

Water was allowed to saturate with $CO_2$ at 100 psig for approximately 19 hours and then injected into the micromodel at 170 psig. After 25 minutes, the pump was used to increase the back pressure. Approximately 2 hours later, the system reached pressure equilibrium and the

experiment was started. At the beginning of the experiment, the pump withdrew fluid at a rate of 0.005 mL/min. At 2 min this rate was changed to 0.0025 mL/min, and at 10 min the rate was changed to 0.004 mL/min. The rate remained at 0.004 mL/min for most of the experiment until 192 min the rate was increased to 0.01 mL/min. At 225 min the rate was increased again, to 0.05 mL/min. The plot of downstream pressure versus time indicates these changes in flow rate. Increasing flow rate results in a greater pressure decline as shown in Fig. 3.1. Unfortunately, 123 minutes into the experiment pressure there was a leak near the upstream pressure gauge. The upstream pressure dropped from 125 psig to 40 psig in a matter of seconds.

### *3.1.1 Pressure Data*

For the first 13 minutes of the experiment the upstream pressure is constant at 170 psig. This is not necessarily indicative of ongoing nucleation. Because of the low fluid withdrawal rate, the low permeability of the micromodel, and the large dead space, it is possible that a disturbance in pressure at the downstream side of the system does not immediately result in a disturbance in pressure at the upstream side of the system. Furthermore, the fact that the pressure in the micromodel is 170 psig greater than the saturation pressure removes the possibility of nucleation at the beginning of the experiment from consideration. With continued volume expansion the upstream pressure begins a steady decline.

Both the upstream and downstream pressures fall abruptly at 123 minutes during the leak near the valve upstream from the pressure vessel. The upstream pressure falls from 125 psig to 40 psig, and the downstream pressure falls from 119 psig to 44 psig. This brings the pressure from above the bubble point to well below it, and the pressure data show that vigorous nucleation, gas-phase expansion, and coalescence of gas bubbles ensue. A strong rebound in pressure is observed in Fig. 3.1, both upstream and downstream after the leak stops. A rebound in pressure is a classic indication of gas phase nucleation and growth. A strong increase in pressure drop that begins at 123 min is displayed in Fig. 3.2. This increase in pressure drop is evidence of a decrease in mobility caused by the appearance and growth of gas bubbles in the pore space. The abrupt increase in the slope of the plot after 123 min is probably due to a portion of the largest pores becoming filled with gas, thereby inhibiting liquid flow. The oscillating pattern on the plot between 10 and 100 minutes is noise in the pressure readings. At 150 minutes,

the downstream pressure begins to decrease again, but the upstream pressure continues to rebound throughout most of the experiment.

### *3.1.2 Visual Data*

Before the volume expansion experiment began, a nucleation site was observed while live water was being injected into the micromodel during steady-state flow. The pressure gradient across the micromodel was 34 psi/cm (a total pressure drop of 170 psi from inlet to outlet). Gas bubbles repeatedly nucleated at the same site. A bubble would expand to fill the pore space after it nucleated, and would eventually be mobilized and flow out of the pore space. Within a fraction of a second after a bubble left the nucleation site more gas would nucleate at the site. The nucleation site is a dirt spot covering part of the pore space. Several sequences of gas bubble nucleation were captured from videotape of the experiment.

There are two methods by which dirt was observed to enter the micromodel. Dust and other particles can easily enter the porous medium before the micromodel is bonded. Dirt was also deposited in the micromodel when gas bubbles dissolved into the liquid phase. A sequence of the formation of a dirt spot was recorded during this experiment.

At the beginning of the sequence (0 s), a gas bubble is observed, as shown in the center of Fig. 3.3a. At 4.2 s, the contraction of the gas bubble due to increasing pressure is evident in Fig. 3.3b. Continuing contraction at 5.53 s is shown in Fig. 3.3c. By 7.77 s, all of the $CO_2$ has dissolved into the liquid phase, and a dirt spot is left behind at the location of complete dissolution, as seen in Fig. 3.3d. Solid particles are attracted to the gas-liquid interface and transported on it as the bubble contracts. When the bubble dissolves completely, the particles are deposited at the location of dissolution. This phenomenon is observed on several occasions in water-$CO_2$ and oil-$CO_2$ systems.

A recorded sequence that displays gas dissolving into solution at the nucleation site is of great interest. This sequence is recorded while increasing back pressure causes the average micromodel pressure to increase. A gas bubble enters solution once the local pressure approaches the saturation pressure. At the beginning of the sequence (0 s), a gas bubble fills several pores, as shown in Fig. 3.4a. The bubble contracts, as observed in Fig. 3.4b at 1 min 53.33 s. Figure 3.4c displays continued contraction due to the increase in pressure by 3 min 5.17 s. At 4 min 5.17 s, the continued contraction of the gas bubble results in snap-off at two pore throats, as shown in

Fig. 3.4d. Carbon dioxide continues to enter solution at 4 min 41.83 s and the bubble continues to contract as seen in Fig. 3.4e. By 4 min 50.67 s, Fig. 3.4f shows that the bubble no longer surrounds the small grain. Figure 3.4g indicates that the gas bubble only occupies the pore at which the nucleation site is located at 5 min 3.67 s. Increased pressure causes all of the gas bubbles in the field of view to contract. Carbon dioxide continues to enter the liquid phase, and at 5 min 38.83 s Fig. 3.4h displays continued contraction of the gas phase. By 5 min 57.67 s, only a small amount of $CO_2$ in the gas phase is visible, as shown in Fig. 3.4i. The $CO_2$ bubble dissolves at 5 min 57.83 s at the exact location of the nucleation site, as indicated by Fig. 3.4j.

The next sequence displays the expansion and mobilization of a recently nucleated gas bubble. At the beginning of the sequence (0 s) a recently nucleated gas bubble is visible, as shown in Fig. 3.5a. The bubble is located on the boundary of the dirt spot, and near a pore wall. By 0.17 s, expansion of the gas bubble is observed in Fig. 3.5b. The bubble at the nucleation site and another bubble to the right expand, as seen at 0.9 s in Fig. 3.5c, and are only separated by a small grain. The bubbles expand enough so that they come into contact and immediately coalesce by 1.2 s, resulting in a single large bubble visible in Fig. 3.5d. The gas expands to fill the pores surrounding the small grain, as observed in Fig. 3.5e, by 2.4 s. Some of the gas flows through a pore throat at 2.8 s, leaving the nucleation site exposed, as observed in Fig. 3.5f.

Another example of bubble growth after nucleation was recorded. A recently nucleated bubble (0 s) is observed, as shown in Fig. 3.6a. By 0.47 s, it is apparent that the bubble is expanding, as observed in Fig 3.6b. Fig 3.6c shows that the bubble fills a pore by 0.77 s. At 1.03 s, Fig 3.6d indicates that the bubble is starting to expand into another pore space.

Nucleation is often observed immediately after a gas bubble vacates the pore in which the nucleation site is located. This repeated nucleation is displayed in a recorded sequence. Figure 3.7a shows a large gas bubble occupying several pores and blocking a nucleation site at the beginning of the sequence (0 s). At 0.033 s the bubble flows through a pore throat and leaves the nucleation site, as shown by Fig. 3.7b. Water fills the space vacated by the bubble. A new $CO_2$ bubble is observed at the nucleation site, as displayed in Fig. 3.7c, at 0.067 s. Carbon dioxide molecules are steadily diffusing to the nucleation site, and as soon as one bubble leaves the site another bubble nucleates and expands. By 0.7 s, part of the large bubble snaps off and leaves the field of view in Fig. 3.7d, and the recently nucleated bubble expands. Continued expansion of all the gas bubbles in the field of view is observed in Fig. 3.7e at 1.3 s.

Another set of nucleation images is given in Fig. 3.8 at 0 s. The nucleation site is occupied by a large gas bubble, as seen in Fig. 3.8a, at the beginning of another sequence of repeated nucleation (0 s). By 0.033 s, the large bubble begins to flow through a pore throat, and the bubble begins to vacate some pore spaces, as shown Fig 3.8b. Fig. 3.8c shows the bubble leaving the nucleation site at 0.067 s. There is no visible gas at the nucleation site. By 0.1 s, a new, small bubble is already forming at the edge of the dirty area in Fig 3.8d. At 0.7 s, expansion of the gas bubble is observed in Fig 3.8e. The gas bubble to the right of the recently nucleated bubble fills many pores at this point, but is about to flow out of this pore space. Expansion continues at 1.73 s. Figure 3.8f shows that the recently nucleated bubble has expanded to fill a pore.

Repeated nucleation was observed at the same site with no pre-existent microbubble visible. At the beginning of another sequence (0 s), the nucleation site appears to be occupied by water, as shown in Fig 3.9a. It is impossible to determine whether or not a gas bubble that is too small to be detected by the microscope exists at the site. The minimum resolution is 1 μm. The dirt spot is clearly defined. At 0.4 s, a gas bubble nucleates at the site, as seen in Fig 3.9b. Expansion is observed in Fig. 3.9c at 0.8 s. The bubble fills the pore space by 1.27 s and expansion continues, as indicated by Fig. 3.9d.

Occasionally, the nucleation site would appear to be free of gas, and in this case it was impossible to determine whether or not there was a gas bubble at the nucleation site that was too small to be detected by the microscope. It was certain, however, that gas dissolved into the liquid phase at the same site at which gas was observed leaving solution with the liquid phase. Based on this observation there is a strong possibility that the nucleation site is a non-water-wet location. The observations made at the nucleation site strongly suggested heterogeneous nucleation. Gas bubbles were often observed dissolving into solution in the middle of pore spaces, even while simultaneously flowing with the liquid phase. This seemed to indicate that the porous medium does not necessarily have a strong effect on the dissolution of gas into the liquid phase. Occasionally, however, gas bubbles were seen dissolving at pore walls, and observations were recorded of a gas bubble dissolving at an identified nucleation site. Furthermore, when gas evolved in the micromodel it was difficult to find nucleation sites. There was no indication of instantaneous nucleation, and there was much evidence that gas nucleation and evolution was strongly influenced by the capillary effects associated with pore geometry.

## 3.2 Water Saturated with $CO_2$ at 110 psig

Water was saturated with $CO_2$ at 110 psig for approximately 3 hours, after which water was allowed to flow through the micromodel. After 21 hours, the injection pressure was increased and back pressure was applied. The system reached pressure equilibrium at 167 psig, at which point volume expansion was initiated. Pressure results are summarized in Figs. 3.10 and 3.11. The initial flow rate was 0.005 mL/min. This was decreased to 0.004 mL/min at 5 min, and decreased again to 0.003 mL/min at 12 min. Late into the experiment, at 395 min, the flow rate was increased to 0.005 mL/min. The rate was increased again at 405 min to 0.01 mL/min, at 435 min to 0.02 mL/min, at 455 min to 0.1 mL/min, and finally at 458 min to 1 mL/min. The flow rate was increased in an attempt to increase the rate of gas bubble expansion. The changes in flow rate at the end of the experiment are indicated by an increase in the slope of the downstream pressure versus time plot, shown in Fig. 3.10.

### *3.2.1 Pressure Data*

During the first two minutes of the experiment the upstream pressure does not decrease, as time is needed for the disturbance in pressure to travel from the downstream end of the micromodel to the upstream end of the micromodel. At 2 min the upstream pressure joins the downstream pressure in a steady decline. At 85 min the slope of the upstream pressure versus time plot begins to decrease. At the same time a steady increase of pressure drop begins, as observed on the plot of pressure drop versus time, shown in Fig. 3.11. Bubble nucleation probably begins at 85 min, at a pressure of 83 psig. Assuming the saturation pressure is 110 psig, the observed supersaturation is 27 psi. The pressure drop increases steadily until the upstream pressure begins to rebound at 198 min. At this time the pressure drop begins to increase quickly. This is probably a relative permeability effect.

### *3.2.2 Visual Data*

Although nucleation was not directly observed in this experiment, gas bubbles were seen as early as 100 min. Regions with relatively high gas saturations within the porous medium were observed without magnification. Most of these regions of high gas saturation appeared as straight lines at approximately 182 min. Throughout the experiment more lines appeared. The lines

thickened, lengthened, and merged together, similar to the ramified growth pattern discussed in Section 1.1. The lines tended to grow toward the outlet channel (Fig. 3.12).

### 3.3 Kaydol Saturated with $CO_2$

An attempt was made to perform a flow-through experiment of the type described by Bora *et al.* (1997). The valve upstream from the pressure vessel remained open, providing constant pressure at the inlet. Fluid was withdrawn from the outlet using a constant flow rate, with the goal of eventually establishing steady-state flow in the system. The experiment did not work because an O-ring leaked. The leak was caused by the use of a vessel lid that was not fabricated to the proper dimensions. The vessel lid was corrected after the problem was identified. The experiment, however, was not a total loss, as some interesting events were recorded. Kaydol was saturated with $CO_2$ at 170 psig for 20 hours. The upstream pressure was held constant at 215 psig throughout the experiment. Fluid was withdrawn at a rate of 0.005 mL/min, and the downstream pressure dropped during fluid withdrawal. Breathing of an oil lens was recorded at 8 min, when the pressure drop across the micromodel was 20 psi (the pressure gradient was 4 psi/cm). Breathing occurred while the local pressure at an oil lens oscillated several times each second. The pressure changes caused the interfaces of the oil lens to move back and forth very quickly. An interesting sequence of gas-phase evolution was recorded at 22 min, when the pressure reached 170 psig.

At the beginning of the breathing sequence (0 s) a gas-oil interface is observed at a pore throat, as shown in Fig. 3.13a. Water resides in a deep crevice adjacent to a large oil-filled pore. The gas-oil and water-oil interfaces move back and forth very quickly due to small but rapid changes in the local pressure. Pressure decreases, and by 0.067 s the gas-oil interface moves toward the large pore, as observed in Fig. 3.13b. At 0.1 s, the interface moves closer to the pore body, as seen in Fig. 3.13c. Fig. 3.13d shows the interface at the opening of the pore throat into the large pore body at 0.133 s. The gas-oil interface reaches its farthest extent at 0.167 s, as shown in Fig. 3.13e. The local pressure begins to increase, and by 0.2 s, Fig. 3.13f indicates that the interface is already driven back to the location in the pore neck that it occupied at the beginning of the sequence. At 0.267 s, the interface is advancing toward the large pore body again as Fig. 3.13g indicates. By 0.333 s, it is clear from Fig. 3.13h that the interface almost reaches the large pore body. This cycle repeats itself several times each second. It is difficult to

see changes in the position of the water-oil interface in this sequence. The water-oil interface is affected by the changes in local pressure, but to a lesser extent than the gas-oil interface.

Bubble growth following nucleation was also seen in this experiment. At the beginning of the gas-phase evolution sequence (0 s) displayed in figure 3.14, a recently nucleated gas bubble is located at a pore wall as shown in Fig. 3.14a. The pore area occupied by gas is outlined. The pressure is 170 psig; the same as the saturation pressure. There is a crevice in the section of the pore wall occupied by a small bubble. At 1 min 31 s, gas expansion is observed in Fig. 3.14b. Fig. 3.14c displays continuing expansion at 2 min 50 s. The bubble almost fills a large pore by 3 min 6.22 s, but, as observed in Fig. 3.14d, begins to flow through a pore throat. At 3 min 8.37 s, gas quickly leaves the pore space, as shown in Fig. 3.14e. By 3 min 8.53 s, Fig. 3.14f indicates that the gas has almost left the pore space.

Unfortunately, no additional recording was performed at this nucleation site. It is interesting, however, that the nucleation site happened to be at a pore wall. The micromodel is water-wet, so it is unlikely that a gas bubble would be found adhering to a pore wall unless the gas bubble had nucleated there.

## 3.4 Kaydol Saturated with $CO_2$ at an Unknown Pressure

An attempt was made to saturate Kaydol with $CO_2$ at 80 psig. The results of this experiment, however, show that the oil was saturated at a much higher, unknown pressure by the time the experiment began. The oil was allowed to saturate for 24 hours at 80 psig before injection into the micromodel at 140 psig was initiated. After 30 hours injection was stopped. Volume expansion was initiated 19 hours later at a rate of 0.0042 mL/min. The saturation pressure of the Kaydol was higher than the intended saturation pressure of 80 psig.

### *3.4.1 Pressure Data*

Upstream pressure versus time is plotted in Fig. 3.15. Initially, the slope of the pressure with respect to time is zero, whereas the plot of pressure drop versus time given in Fig. 3.16 clearly indicates that mobility decreased from the beginning of the experiment. The two graphs suggest that gas bubbles were present in the porous medium at the beginning of the experiment. Relative permeability effects probably cause the increase in the slope of the pressure drop versus time plot beginning at 10 min. No pressure rebound is observed during this experiment. At 140

min the presure drop begins to decrease, probably due to the mobilization of gas bubbles upon reaching $S_{gc}$. At 140 min the upstream pressure is 128 psig and the downstream pressure is 65 psig. The pressure drop continues to decrease until the end of the experiment at 795 min.

## 3.5 Kaydol Saturated with $CO_2$ at 100 psig or Higher

A pressure decline experiment was performed using a Kaydol-$CO_2$ system. Kaydol was allowed to saturate with $CO_2$ for 22 hours at 100 psig. The pressure was increased to 140 psig, and oil injection was initiated into the micromodel. The valve upstream from the micromodel was shut 47 hours after injection began, and the outlet pressure was increased. By this time the forward pressure had increased to 220 psig due to a faulty pressure regulator. A leak upstream of the pressure vessel began to affect the system. Three hours after the outlet pressure was increased volume expansion was initiated at a rate of 0.006 mL/min in order to achieve pressure decline. The inlet and outlet pressures were not the same. The initial upstream pressure was only 123 psig due to the leak, and the downstream pressure was 110 psig. The upstream pressure had dropped almost 100 psi in three hours because of the leak.

### *3.5.1 Pressure Data*

The fast leak upstream of the micromodel caused the upstream pressure to drop from 123 psig to 100 psig, as observed in Fig. 3.61, within the first five minutes of the experiment before being fixed. Nucleation occurs at 5 min as the flat slope of the upstream pressure versus time plot and the rebound in the slope of the pressure drop versus time plot indicate (Figs. 3.17 and 3.18). Whether or not 100 psig is the actual saturation pressure is difficult to determine because of the long period of time during which the Kaydol was under pressures significantly higher than the intended saturation pressure. It is possible that $CO_2$ diffuses quickly such that during the 47 hour injection period the saturation pressure of the oil increases. From 65 min to 80 min the upstream pressure drops, but at the end of this period the pressure decreases slowly.

## 3.6 Kaydol Saturated with $CO_2$ at 100 psig

This experiment was another attempt to perform a flow-through experiment similar to that of Bora *et al.*, 1997. Due to a faulty pressure regulator, the upstream pressure drifted upward uncontrollably, from 100 psig to 180 psig, before the experiment and made it difficult to

establish a saturation pressure. A volume expansion rate of 0.006 mL/min was used throughout the experiment. The downstream pressure never stabilized because this flow rate was high. The high viscosity of the oil results in a large pressure drop during volume expansion. Thus, the goal of achieving steady-state flow in the micromodel was not accomplished.

Indeed, the pressure data in Fig. 3.19 show that gas is present in the micromodel from the beginning of the experiment. This conclusion is supported by the visual observation of gas in the porous medium just thirty minutes into the experiment. The plot of pressure drop versus time in Fig. 3.20 indicates that around 10.5 min gas bubbles are blocking many flow channels, as evidenced by an increase in the slope of the plot. The rebound in the upstream pressure, beginning at 60 min in Fig. 3.19, is due to pressure drift caused by the upstream pressure regulator.

Interesting visual observations of gas flow from the porous medium into the outlet channel are recorded. When gas bubbles come into contact in water-$CO_2$ systems, the gas bubbles immediately coalesce. During this experiment with a much more viscous liquid, however, the coalescence of gas bubbles does not occur immediately upon contact. Thin-liquid films between bubbles show greater strength than expected. Several observations were made of gas bubbles in contact being squeezed together, and gas-oil interfaces deforming without coalescing. Examples are given in Figs. 3.21, 3.22, and 3.23. The gas bubbles are in contact with each other for minutes at a time before coalescence is observed.

The strength of the gas-liquid interface for Kaydol could be explained if surfactants were present in the solution. During this study, no surfactants were added to any of the solutions used, and no surfactants had ever been used in the micromodels used during the study. The only way surfactant could be in the Kaydol is if the Kaydol was manufactured with the addition of surfactants or if the mineral oil contained trace amounts of surfactant. If this was not the case, the increased gas-liquid interface strength is most likely due to the viscosity of the Kaydol. This finding may have implications for the debate concerning the nature of foamy oil. One hypothesis regarding foamy oil is that the high viscosity of heavy oils inhibits the coalescence of gas bubbles, resulting in the production of a oil-base foam that resembles chocolate mousse upon depressurization.

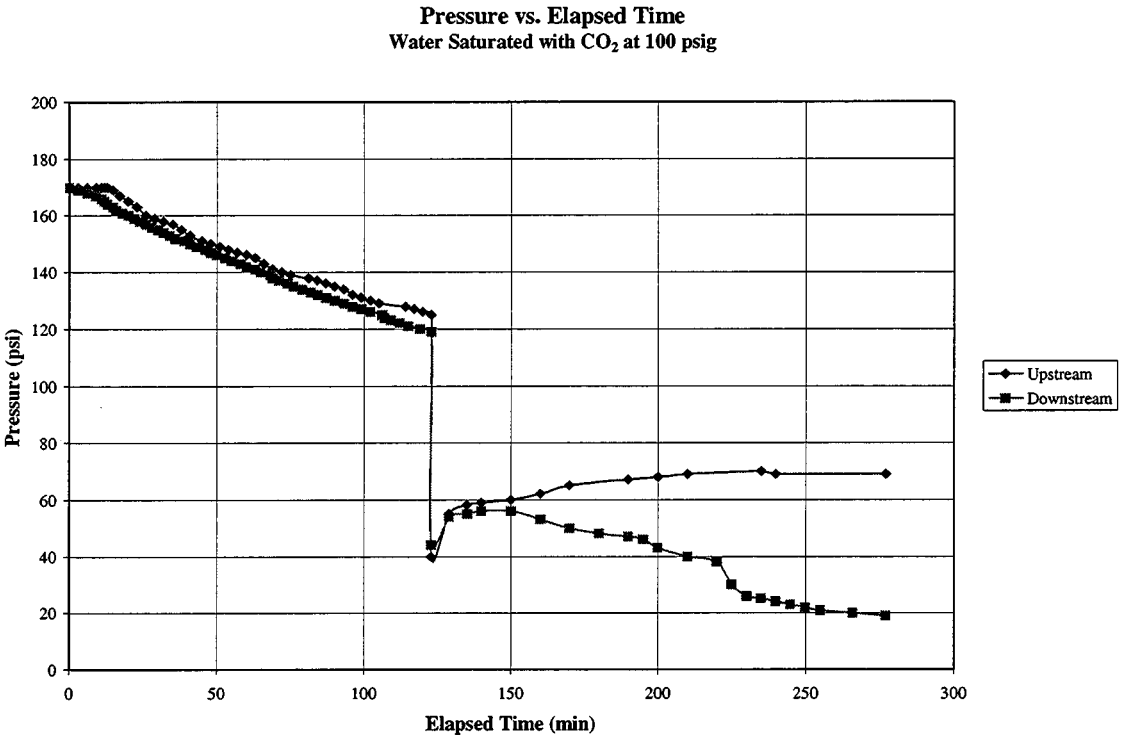


**Figure 3.1: Pressure versus time for water saturated with $CO_2$ at 100 psig.**

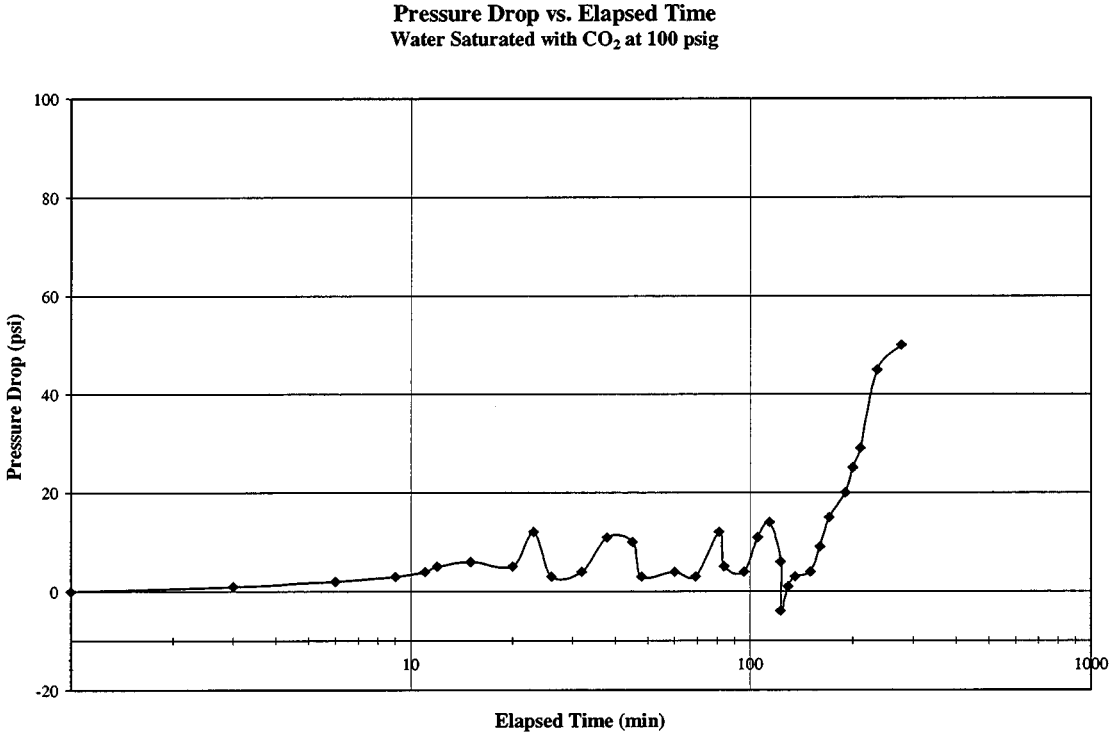


**Figure 3.2: Pressure drop versus time for water saturated with $CO_2$ at 100 psig.**

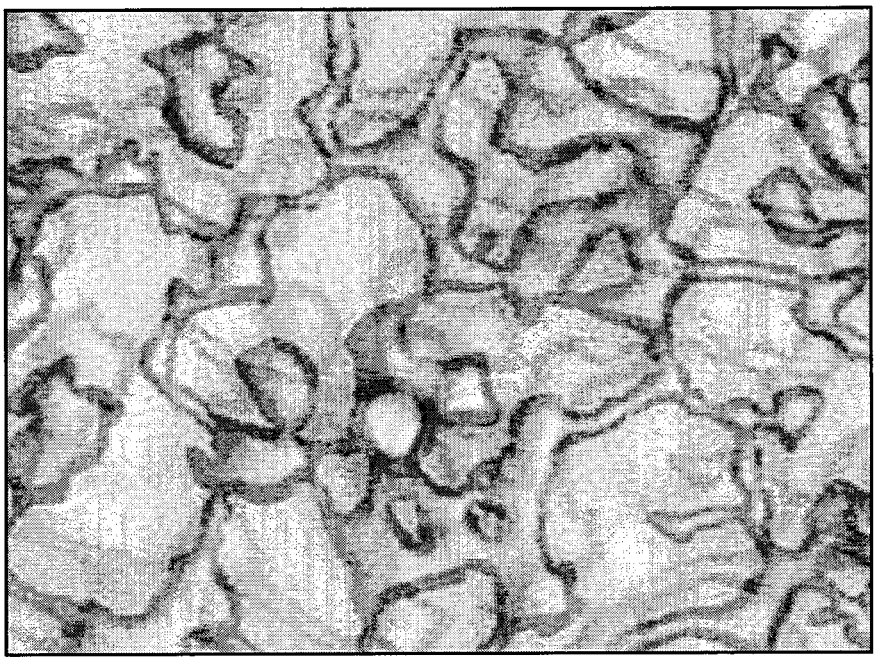

**Figure 3.3 a: Gas bubble.**

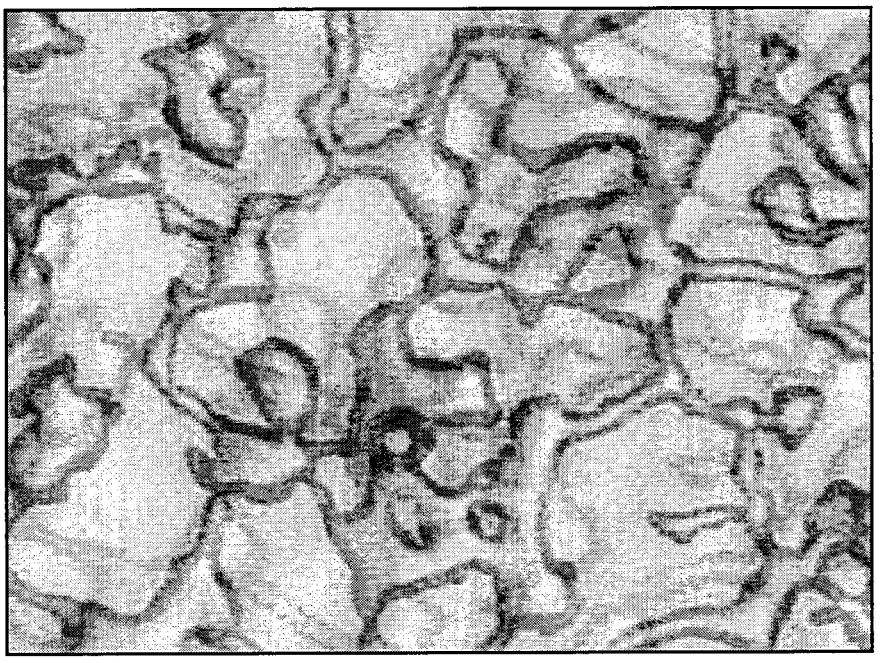

**Figure 3.3b: Gas bubble during contraction.**

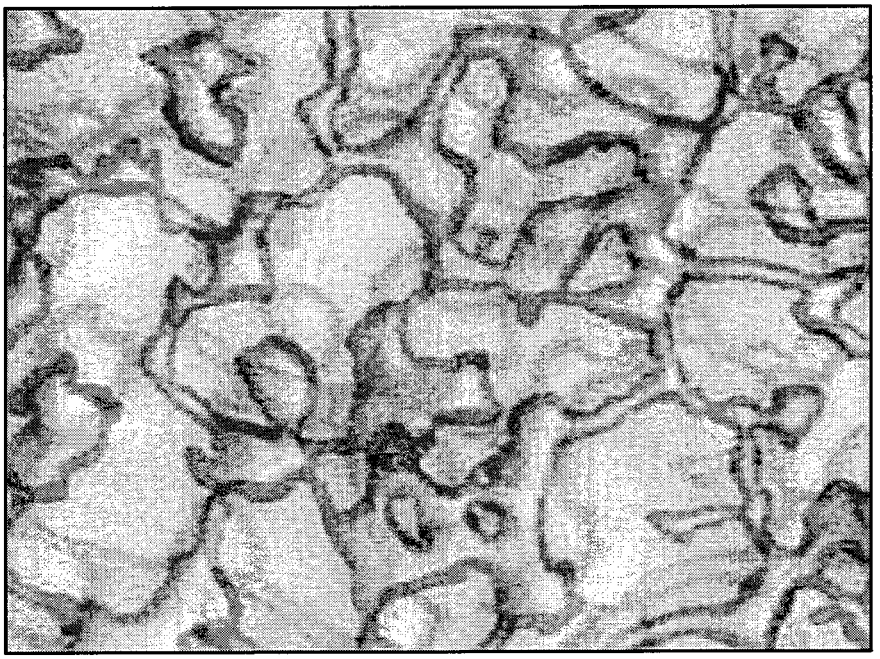

**Figure 3.3c: Gas bubble after significant contraction.**

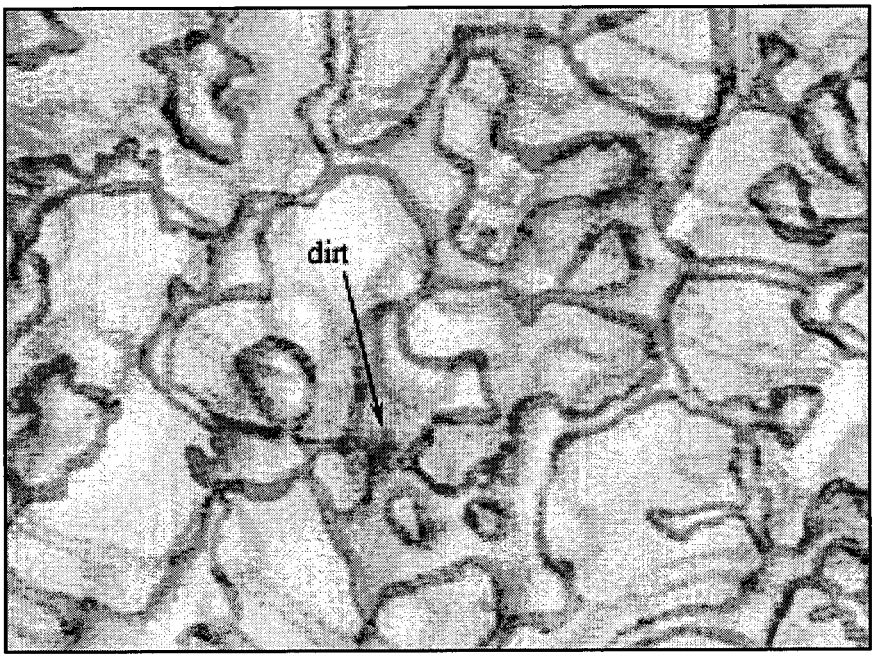


**Figure 3.3d: Dirt spot left behind after the bubble completely dissolved.**

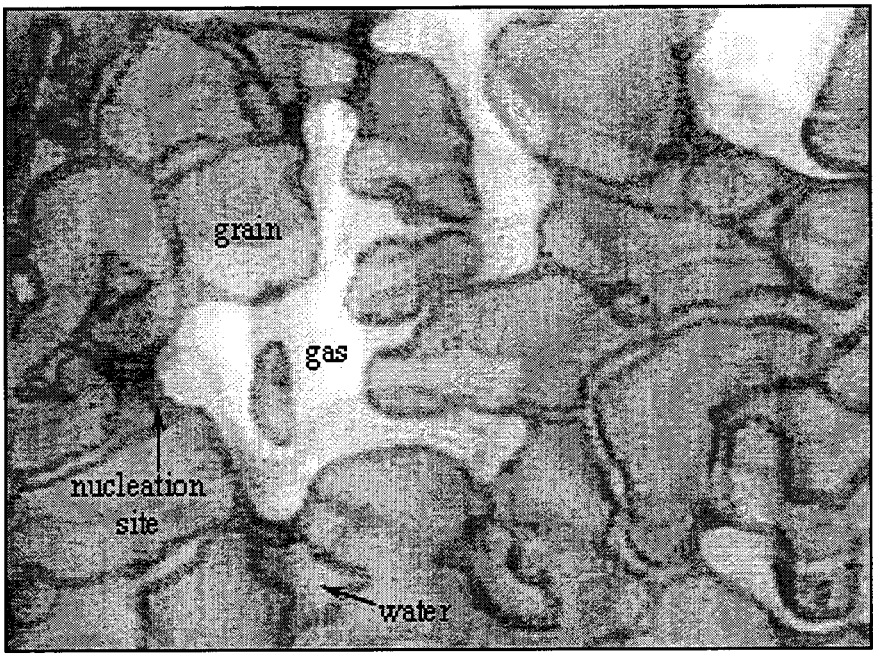


**Figure 3.4a: A large bubble occupies several pore spaces.**

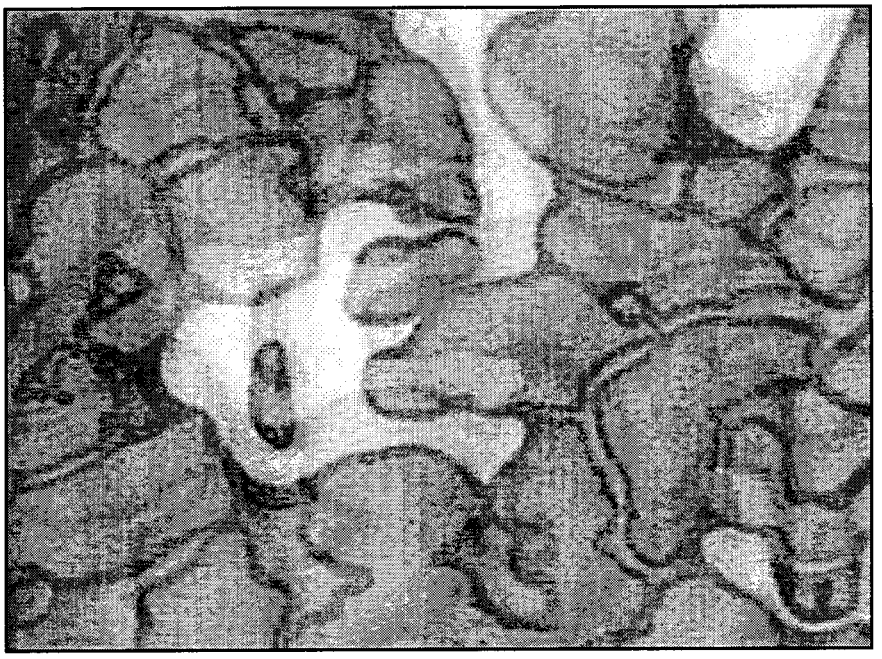

**Figure 3.4b: The bubble contracts and leaves a pore space.**

**Figure 3.4c: Contraction continues.**

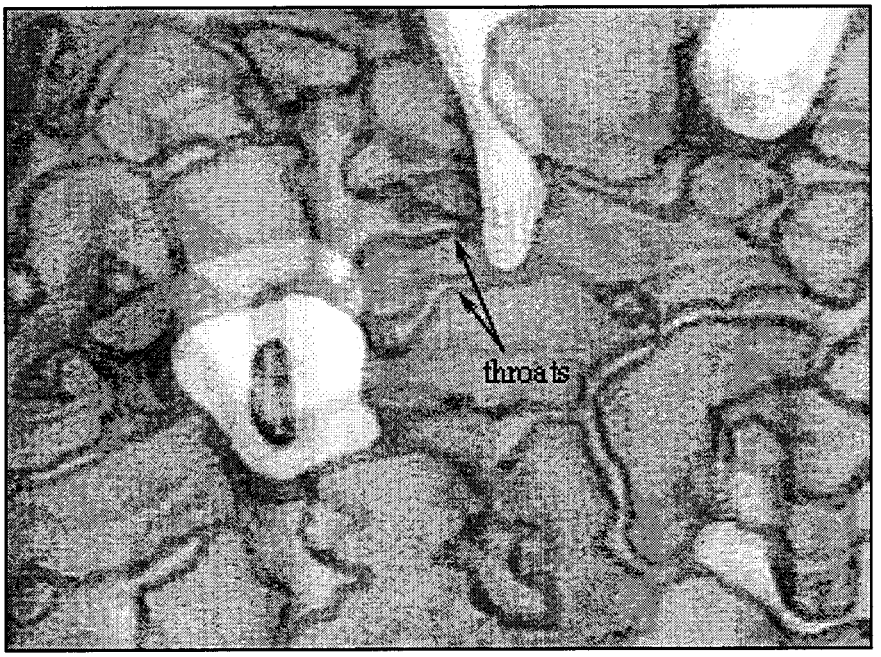


**Figure 3.4d: Snap-off occurs at two pore throats.**

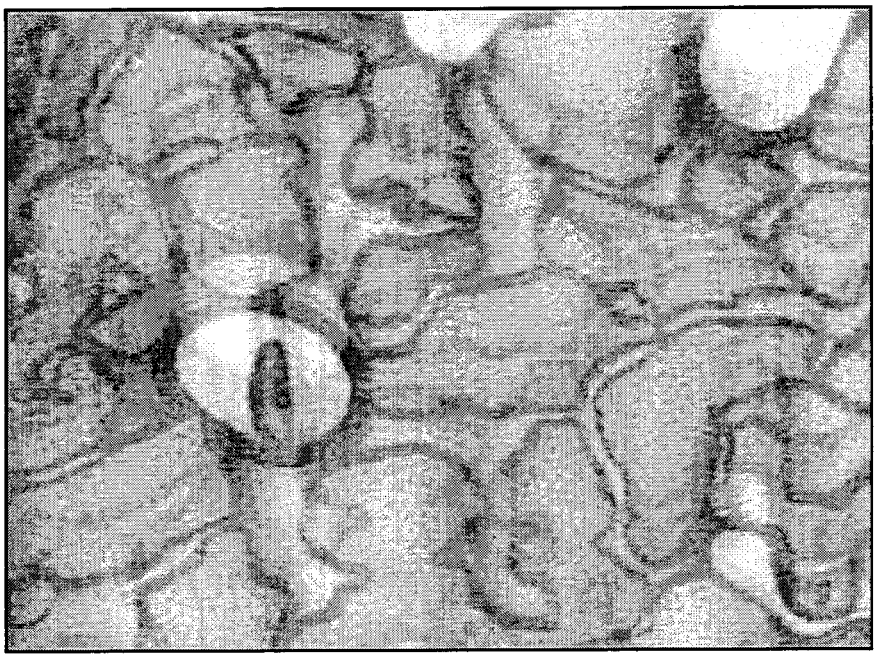

**Figure 3.4e: The bubble continues to contract.**

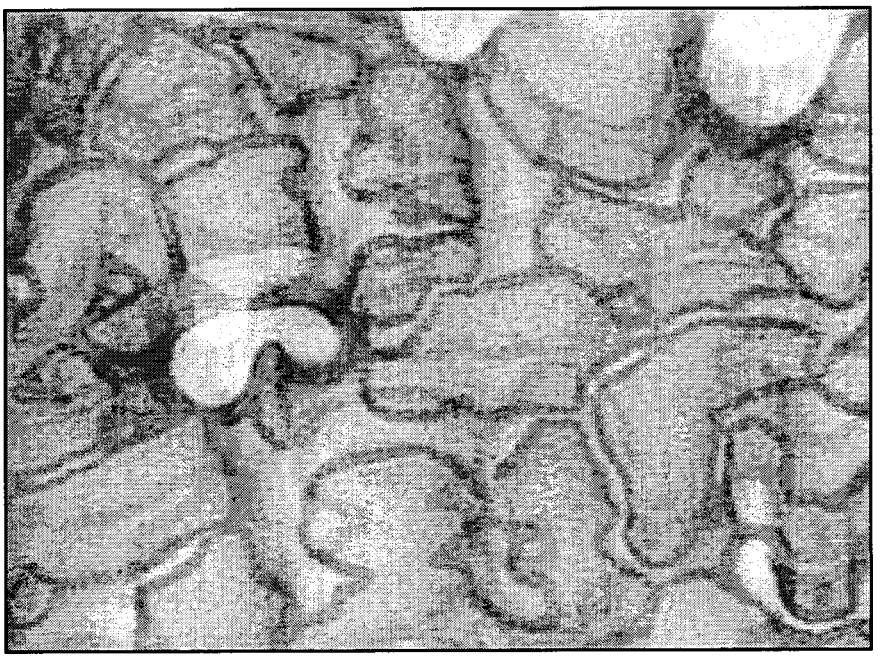

**Figure 3.4f: Contraction continues.**

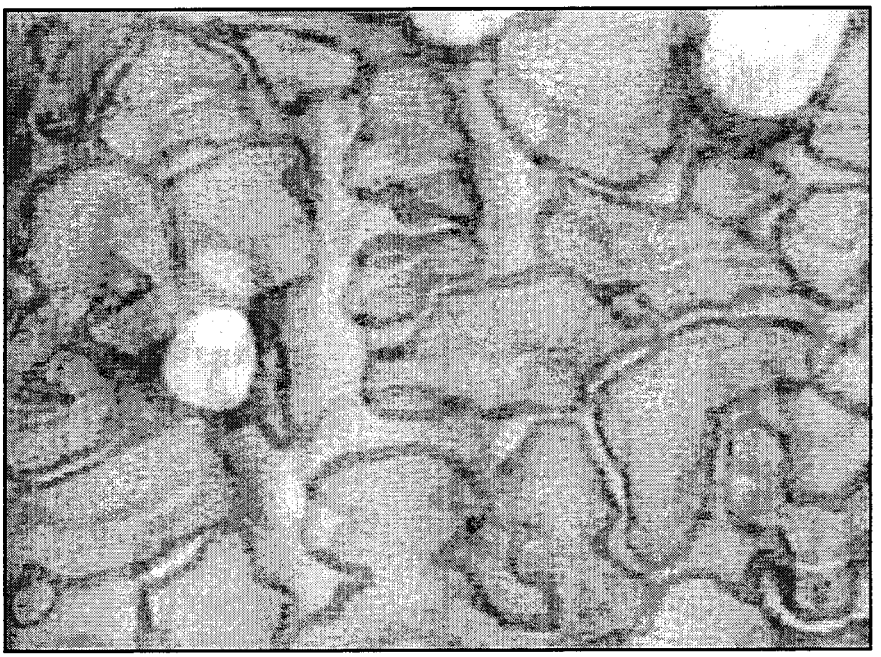

**Figure 3.4g: The bubble only fills the pore in which the nucleation site is located.**

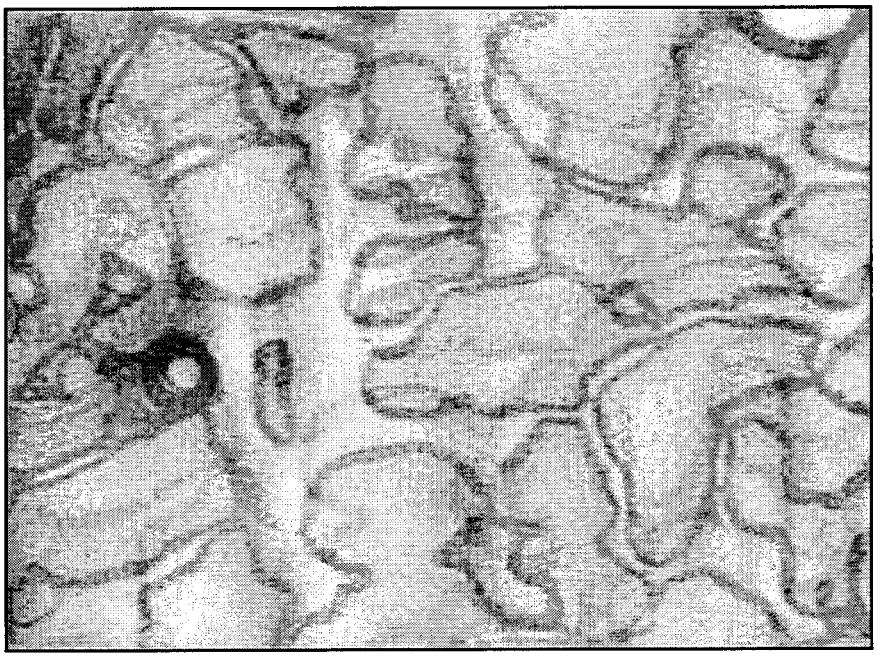

**Figure 3.4h: The bubble contracts, but still occupies the nucleation site.**

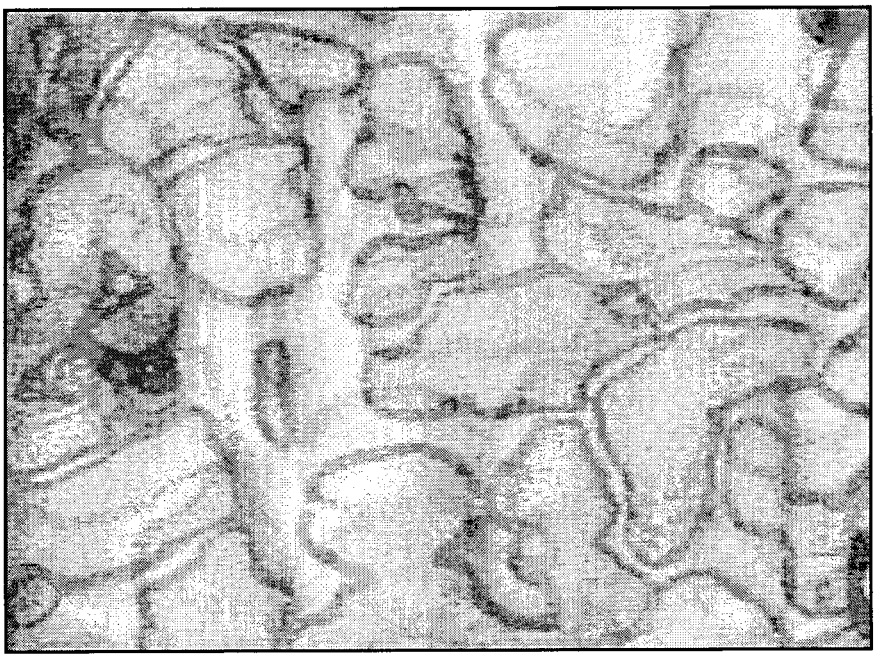

**Figure 3.4i: The bubble is almost completely dissolved.**

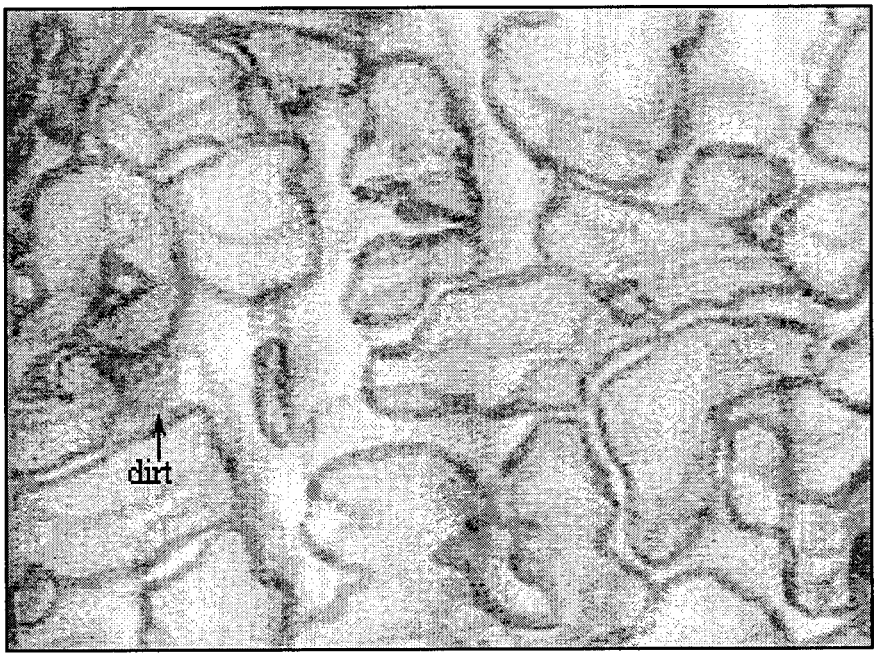


**Figure 3.4j: The bubble disappears at the nucleation site.**

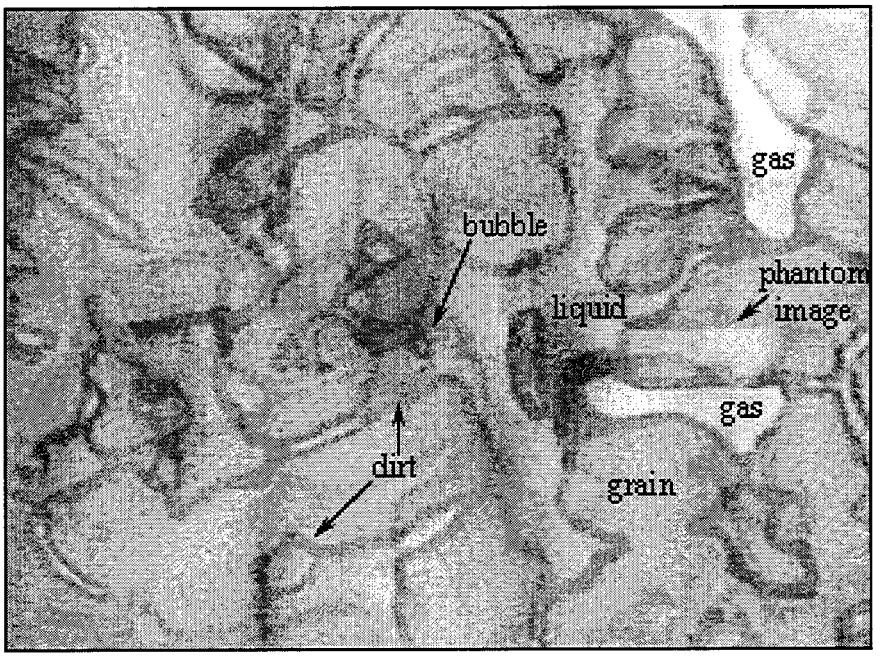


**Figure 3.5a: Recently nucleated gas bubble.**

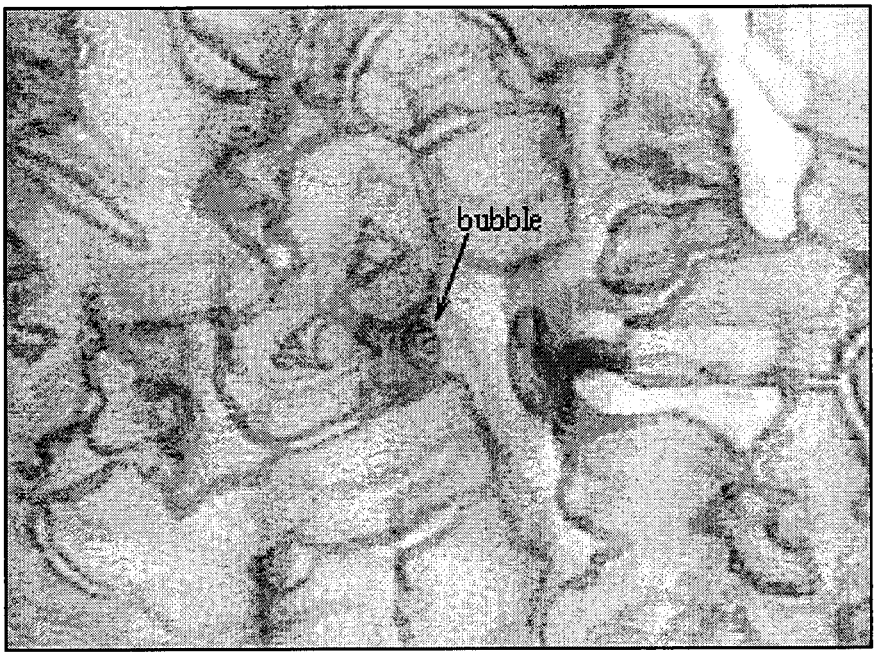


**Figure 3.5b: Gas bubble after expansion.**

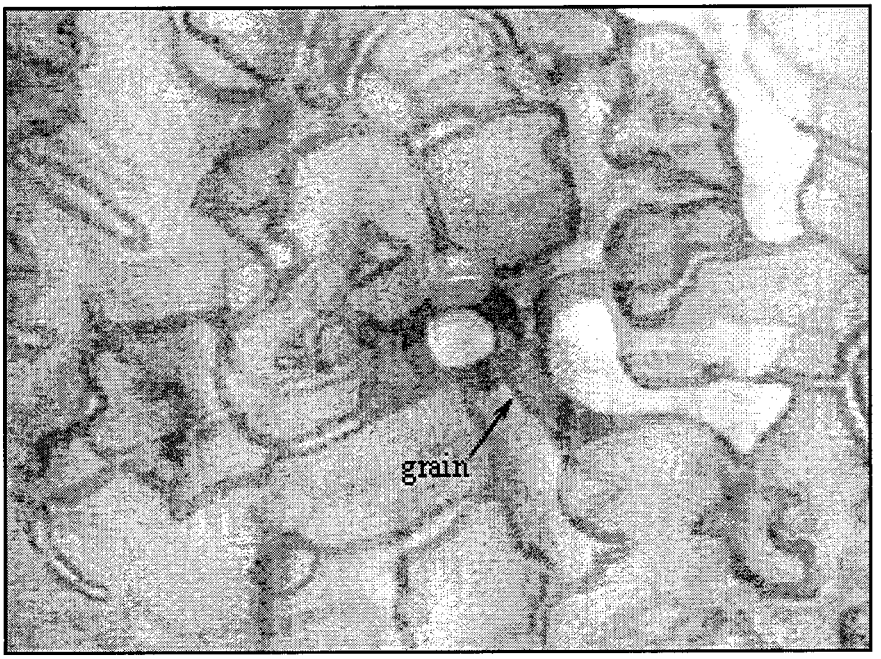


**Figure 3.5c: Gas bubbles separated by a small grain.**

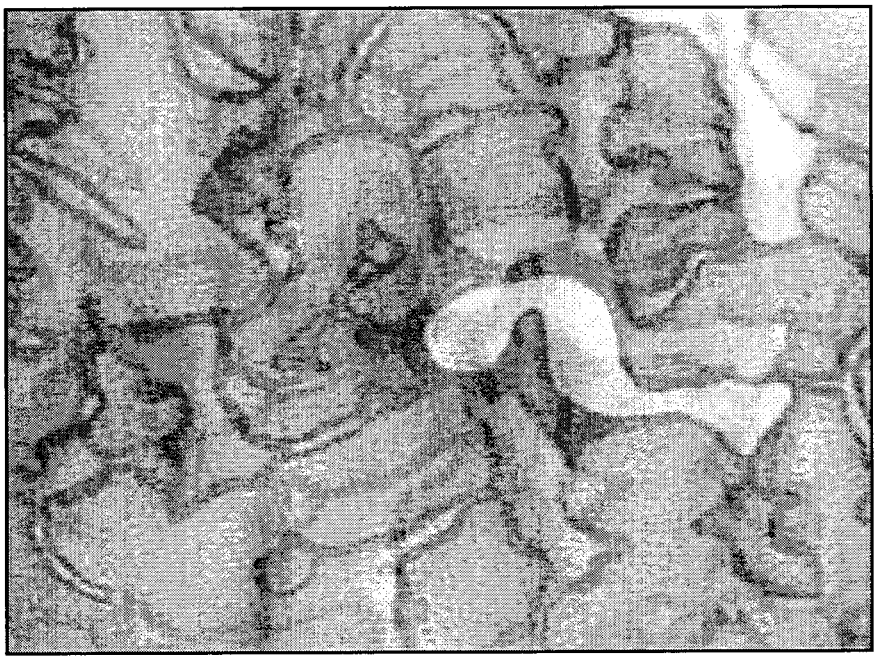

**Figure 3.5d: Bubble after coalescence.**

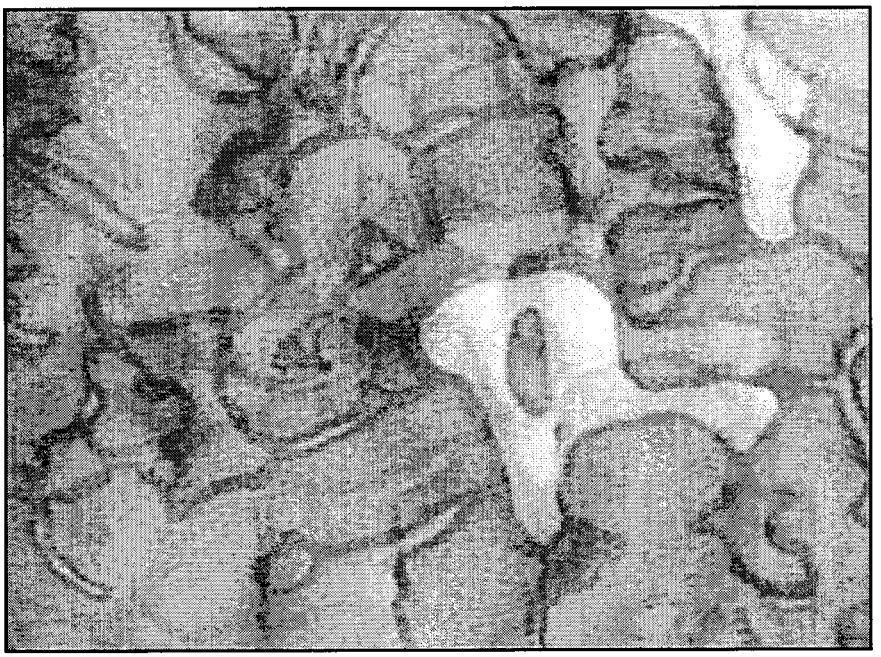

**Figure 3.5e: The gas bubble fills several pore spaces after expansion.**

**Figure 3.5f: Gas leaves the nucleation site.**

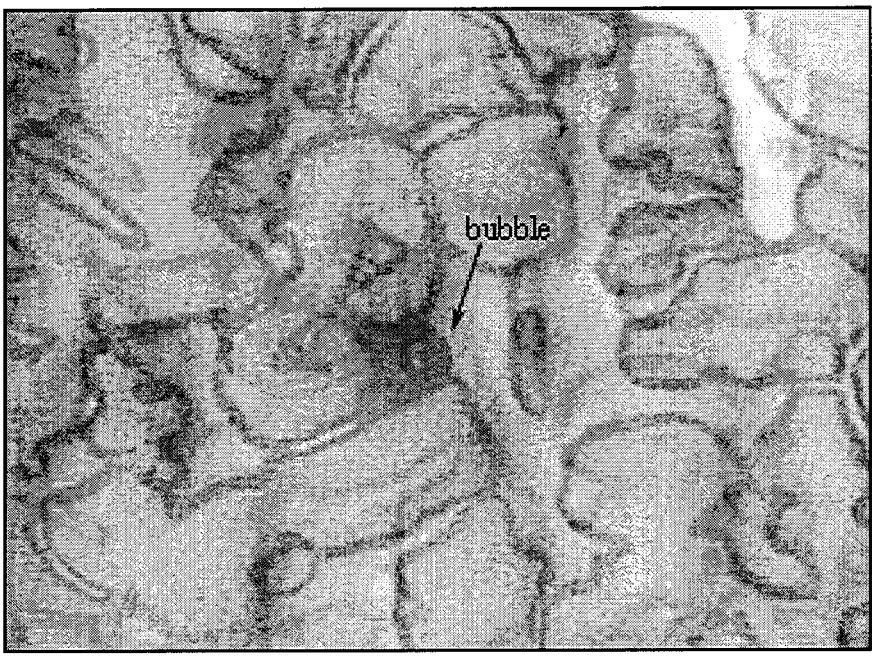


**Figure 3.6a: Recently nucleated gas bubble.**

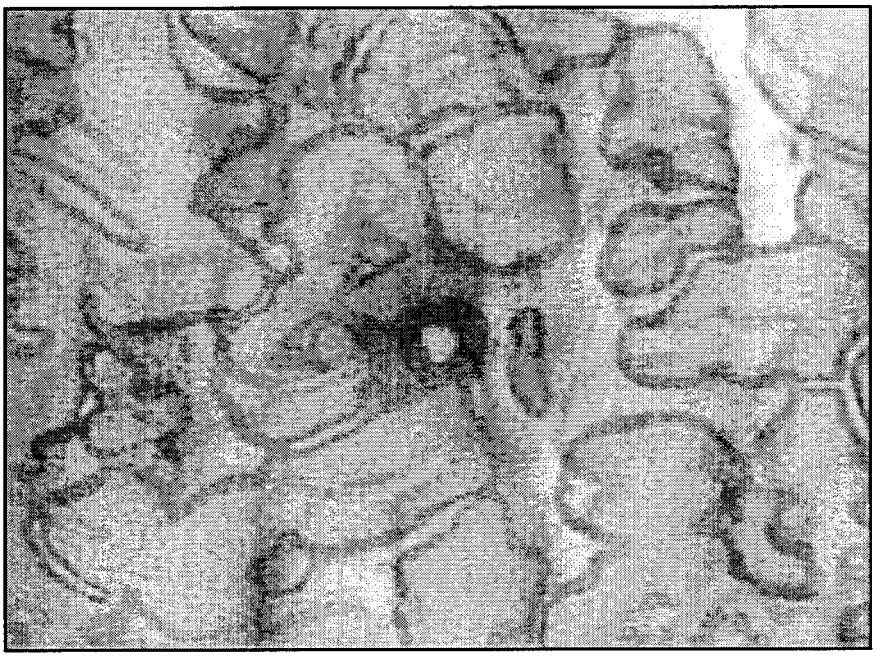

**Figure 3.6b: Gas bubble expands.**

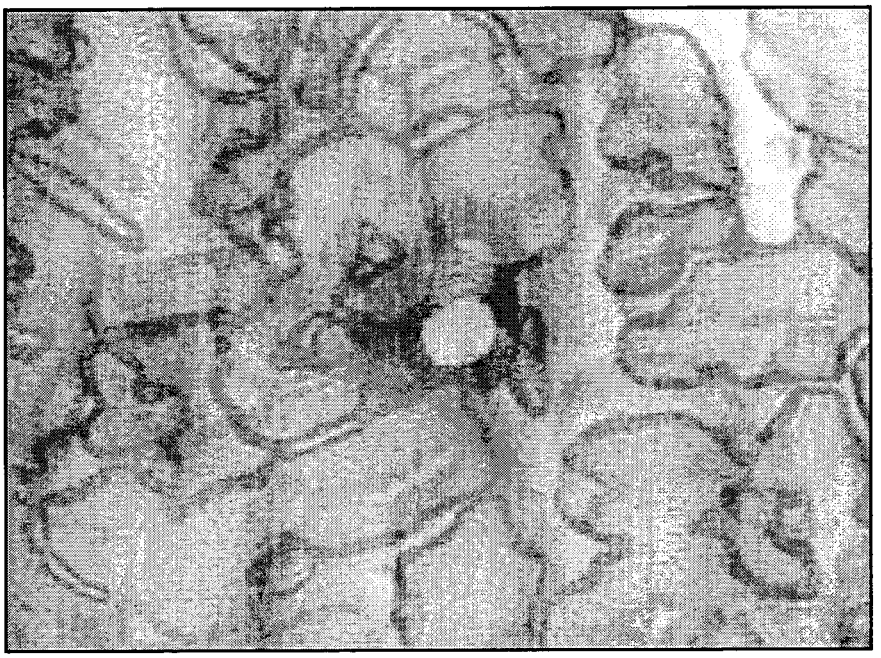

**Figure 3.6c: Gas fills the pore at which the nucleation site is located.**

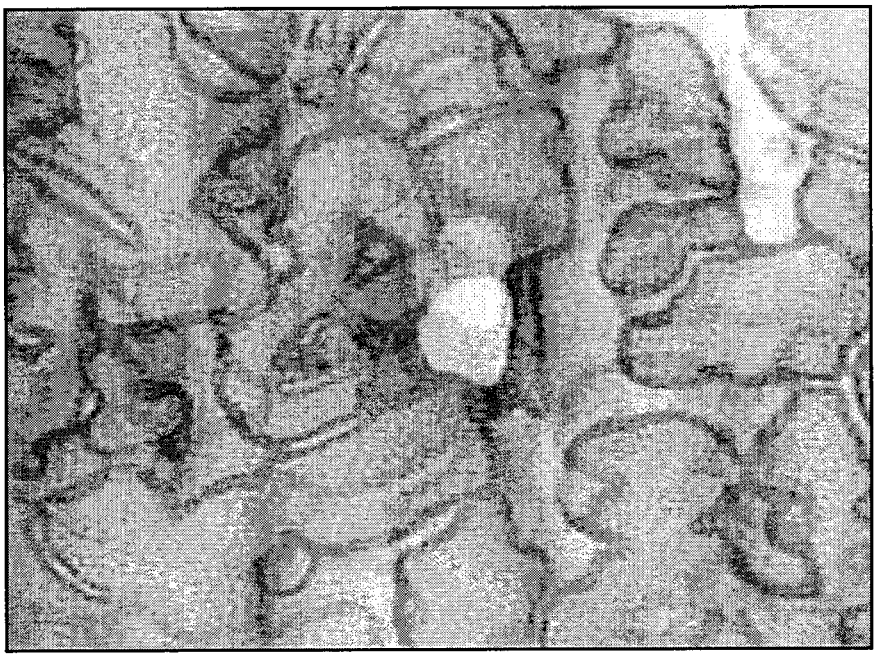

**Figure 3.6d: The gas bubble is about to expand into other pores.**

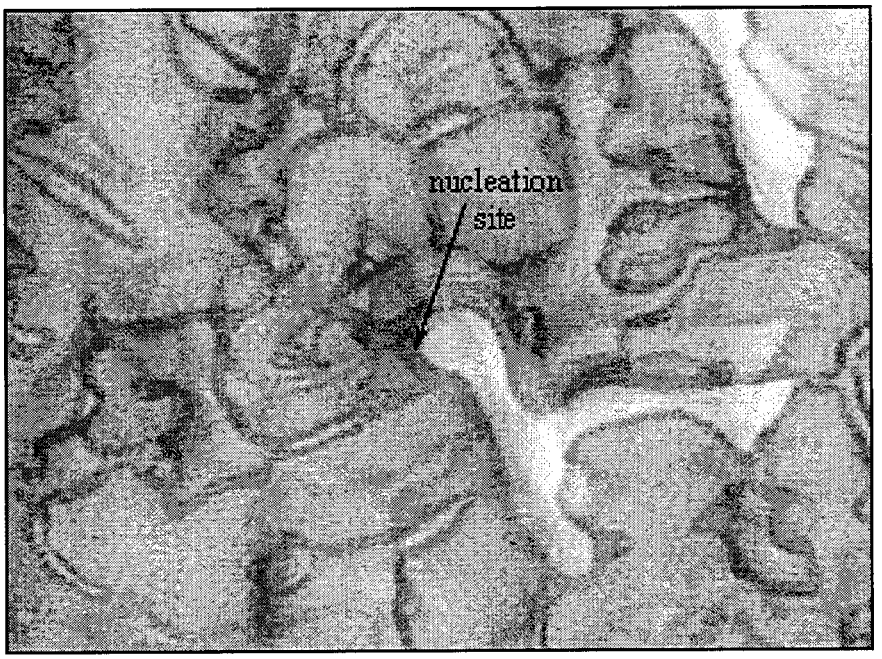


**Figure 3.7a: A bubble occupies the nucleation site.**

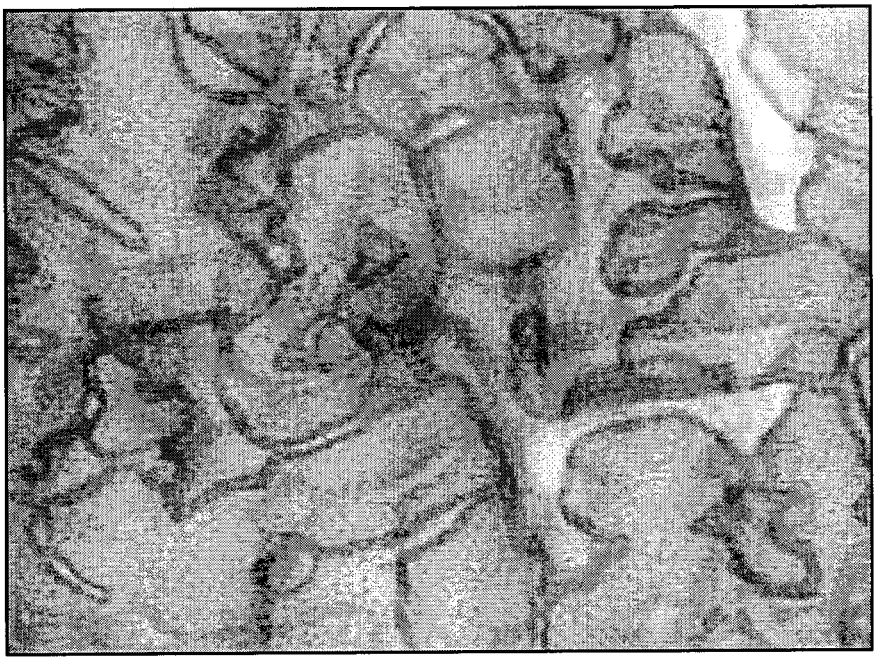

**Figure 3.7b: The bubble leaves the nucleation site.**

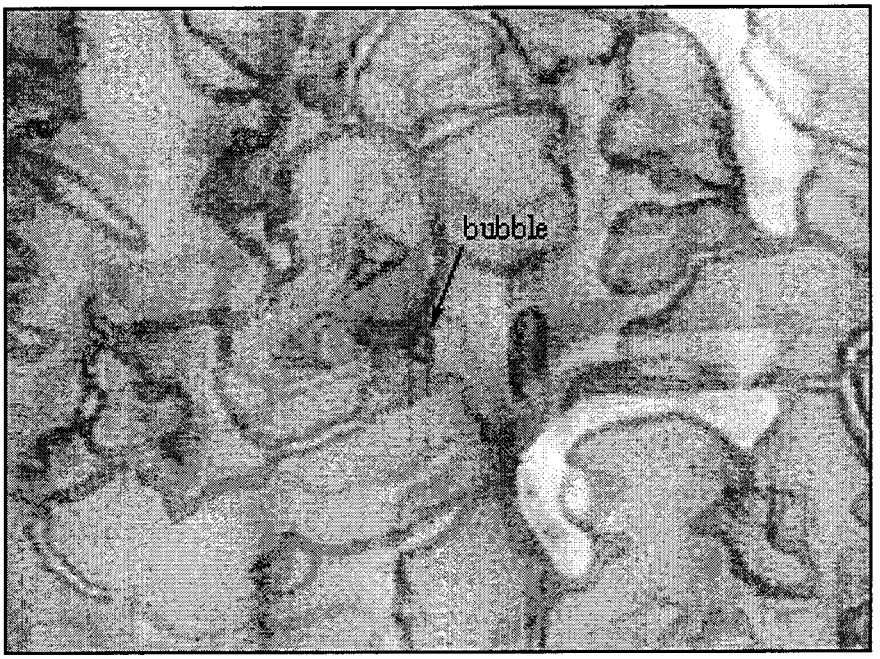


**Figure 3.7c: A new bubble begins to form at the nucleation site.**

**Figure 3.7d: The new bubble expands.**

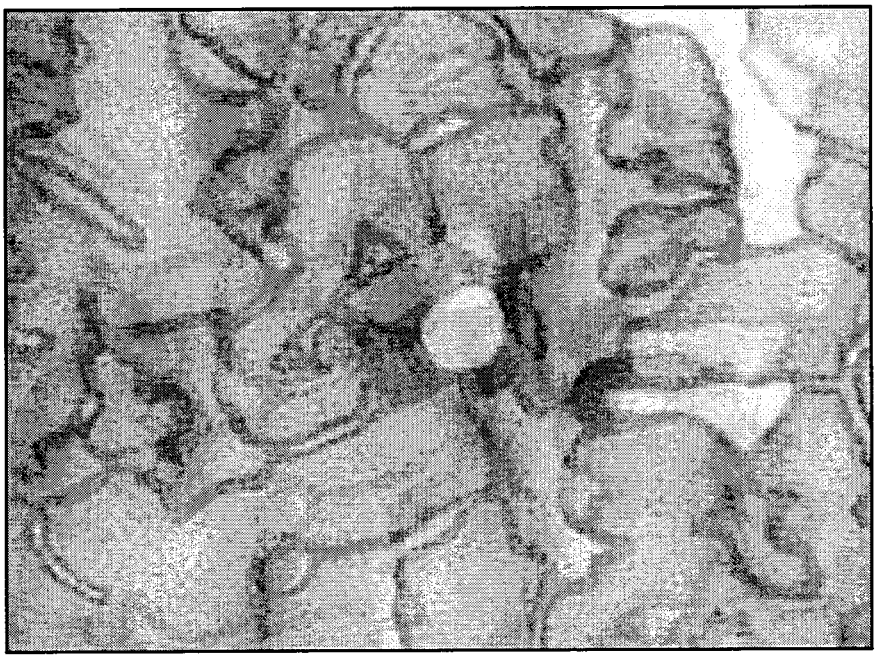

**Figure 3.7e: The bubble expands to fill the pore space.**

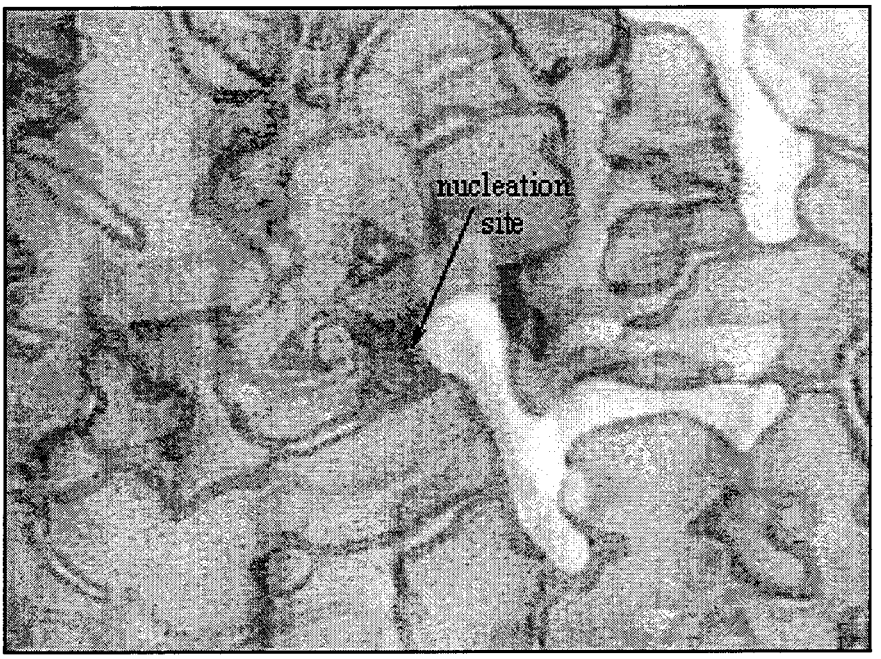


**Figure 3.8a: A large gas bubble occupies the nucleation site.**

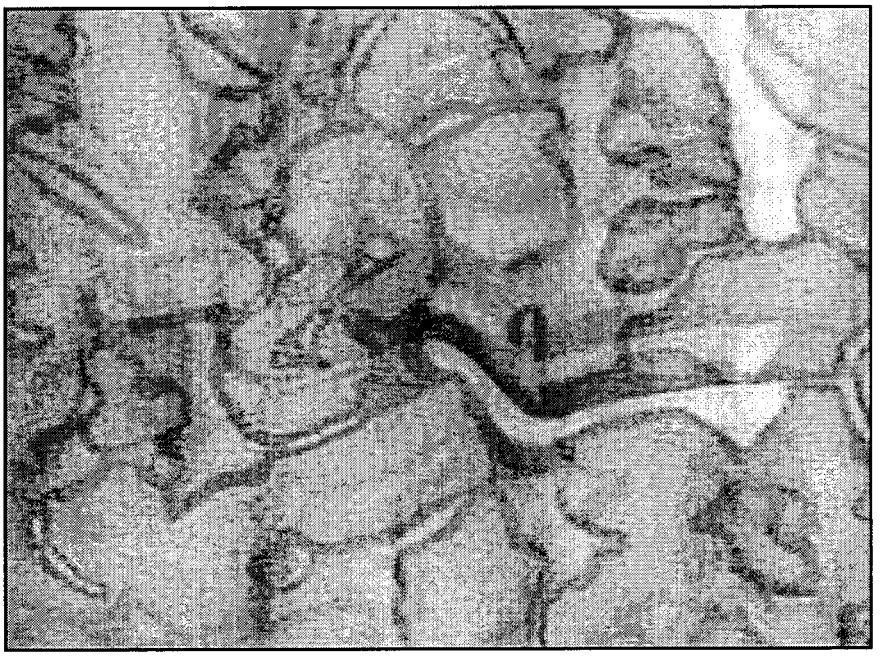

**Figure 3.8b: The bubble begins to flow out of the pore spaces.**

**Figure 3.8c: The bubble vacates the nucleation site.**

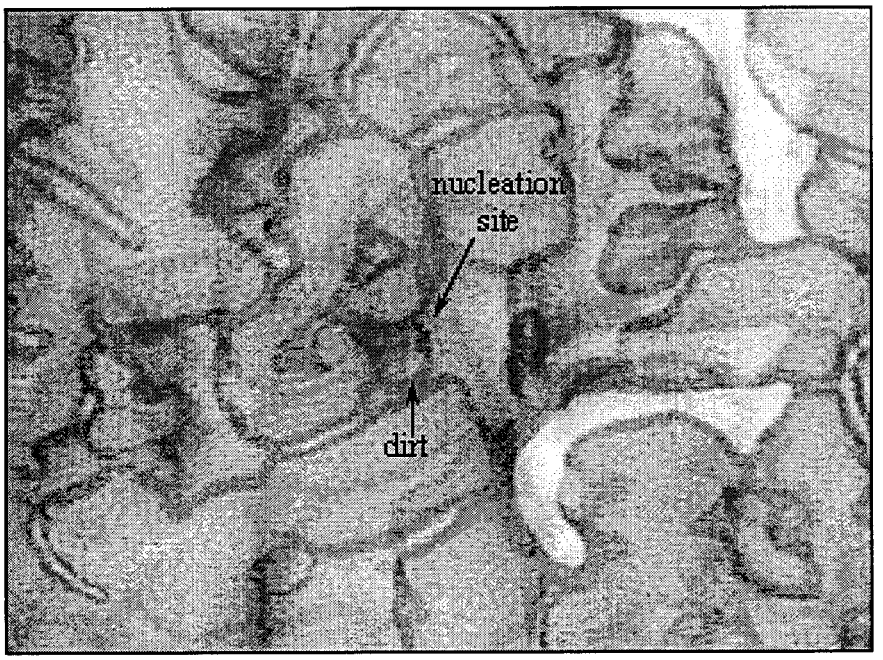


**Figure 3.8d: The nucleation site is free or is almost free of gas.**

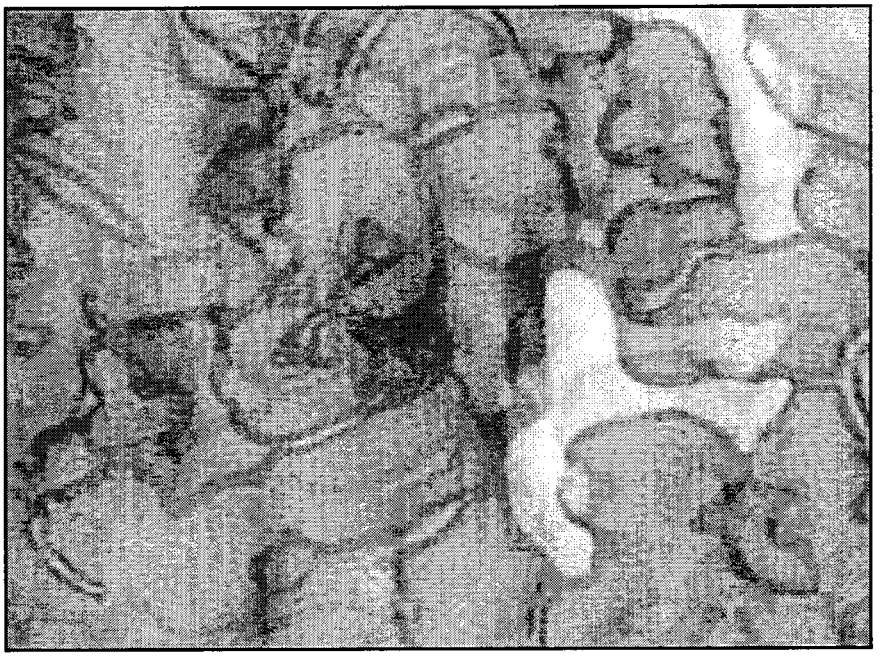

**Figure 3.8e: The new gas bubble expands.**

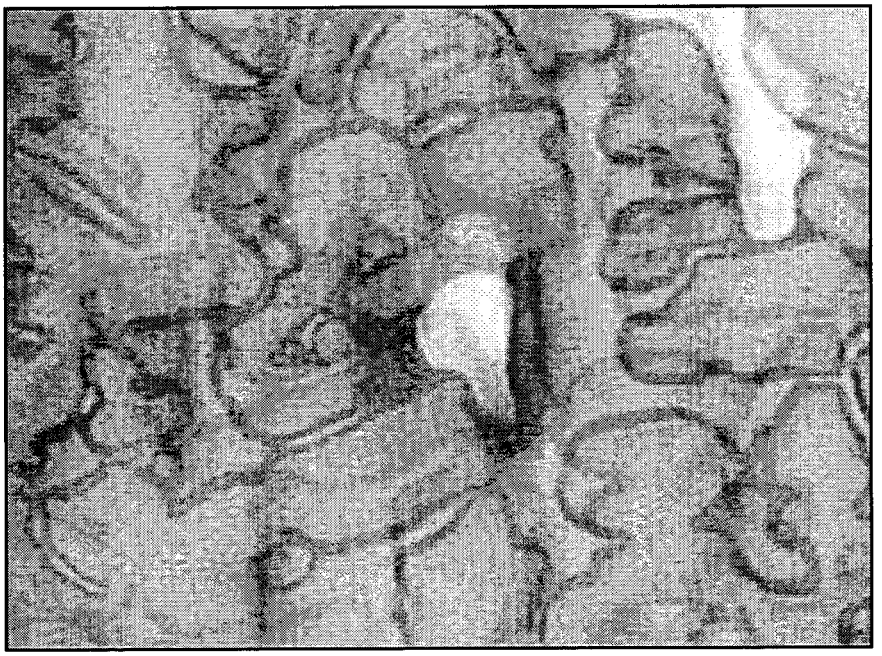

**Figure 3.8f: The gas bubble fills a pore, and is about to expand into a new pore space.**

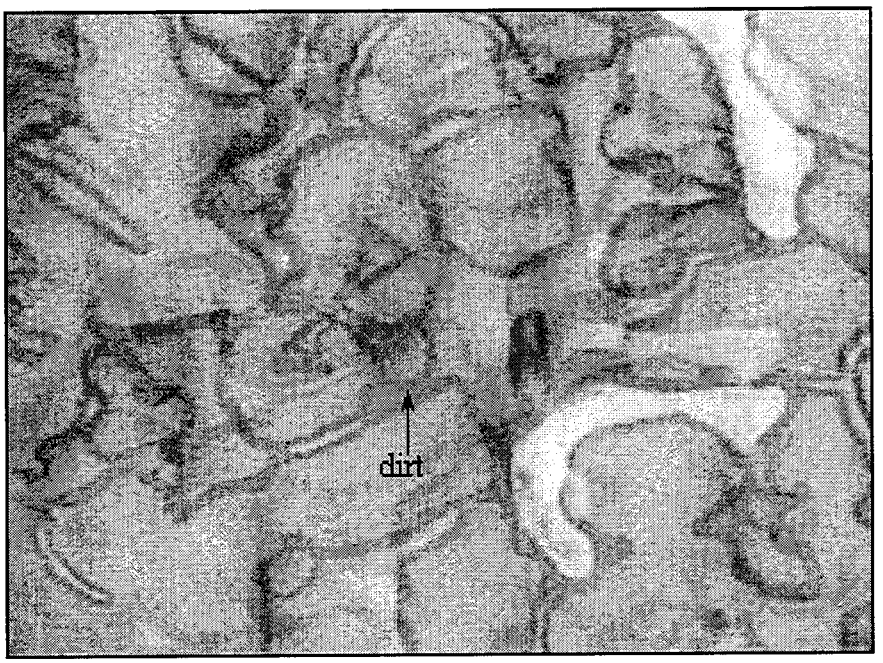


**Figure 3.9a: There is no gas visible at the nucleation site.**

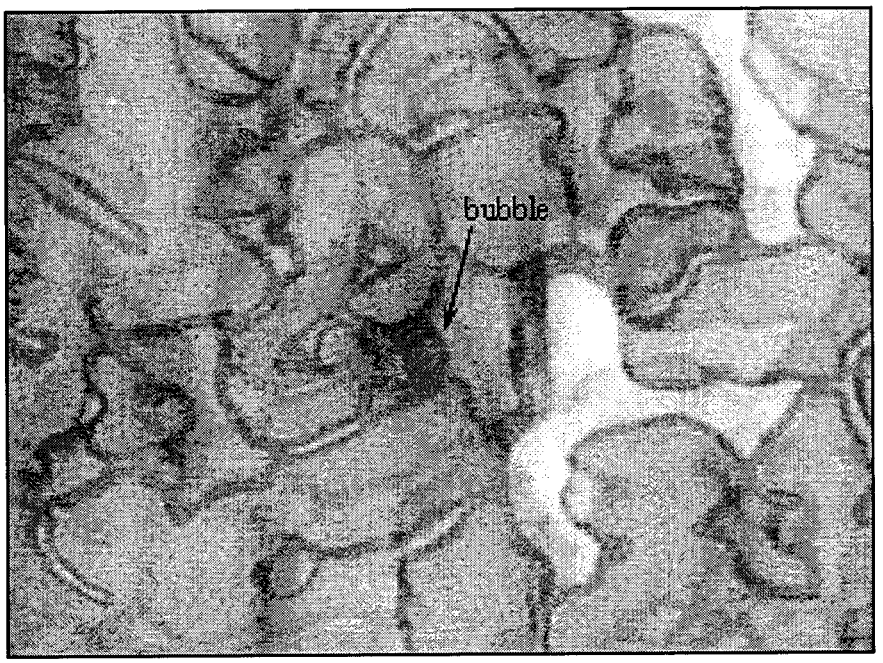


**Figure 3.9b: A bubble nucleates and expands at the nucleation site.**

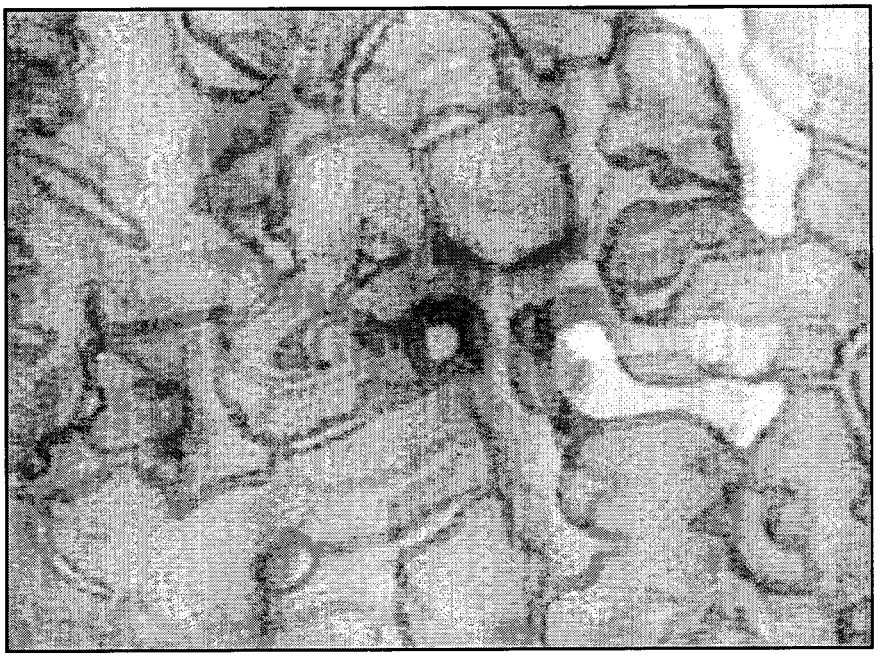

**Figure 3.9c: The new bubble expands.**

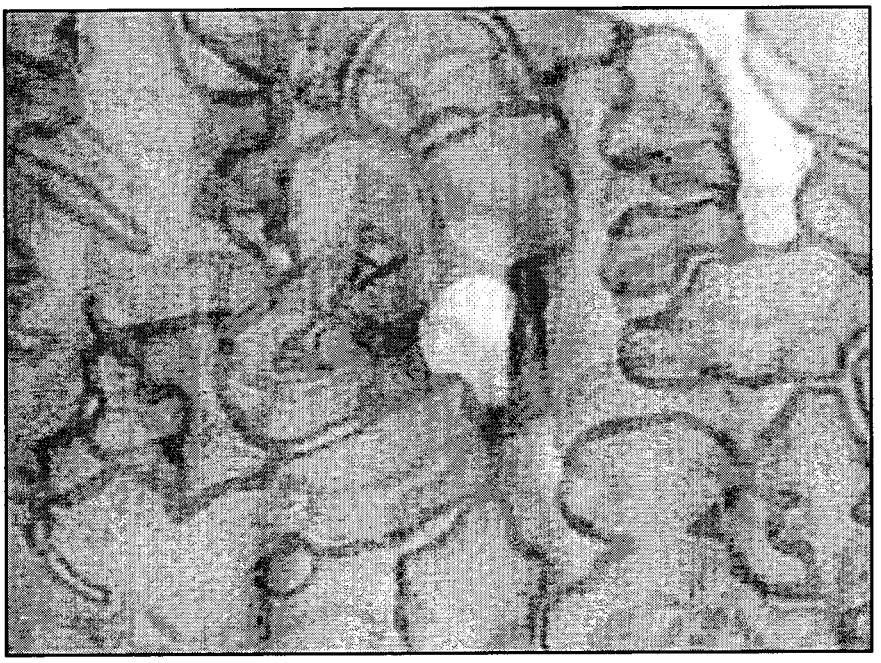

**Figure 3.9d: The bubble fills a pore.**

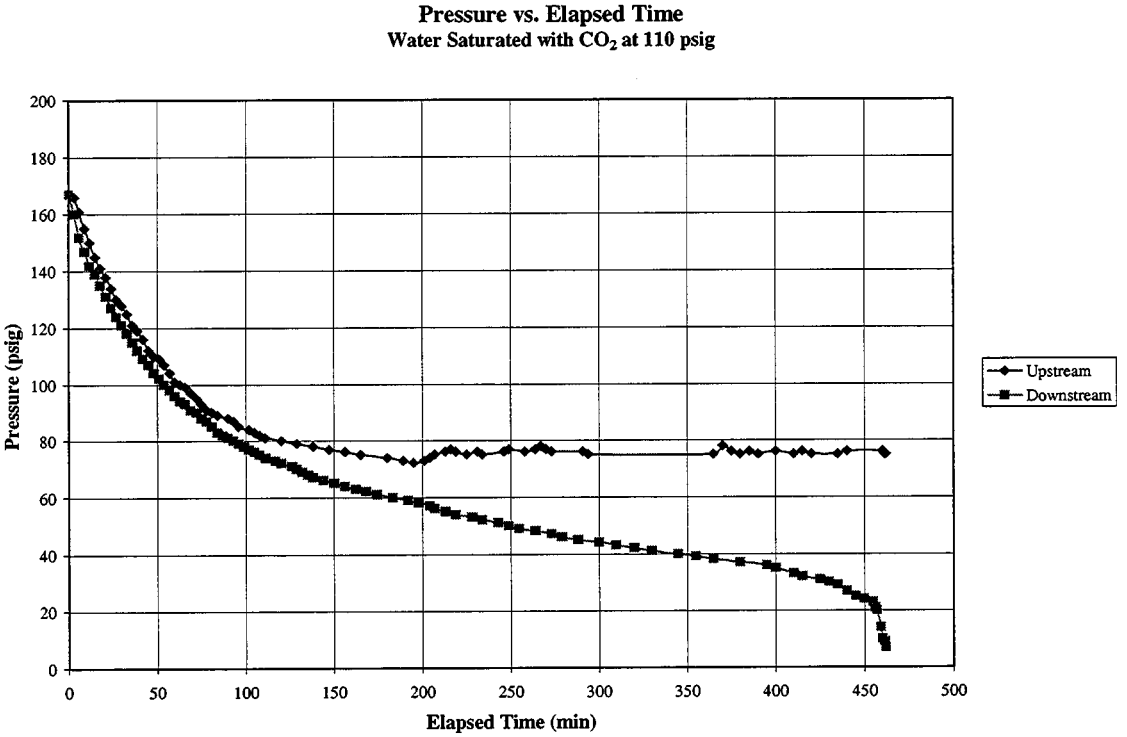


**Figure 3.10: Pressure versus time for water saturated with $CO_2$ at 110 psig.**

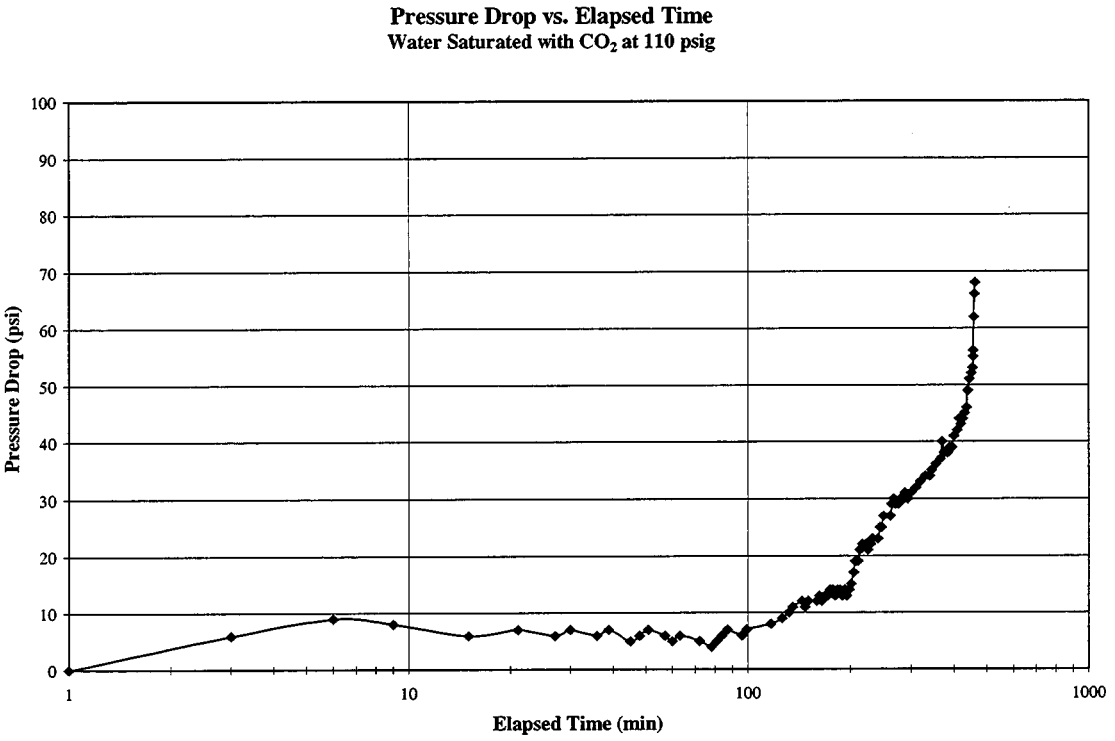


**Figure 3.11: Pressure drop versus time for water saturated with $CO_2$ at 110 psig.**

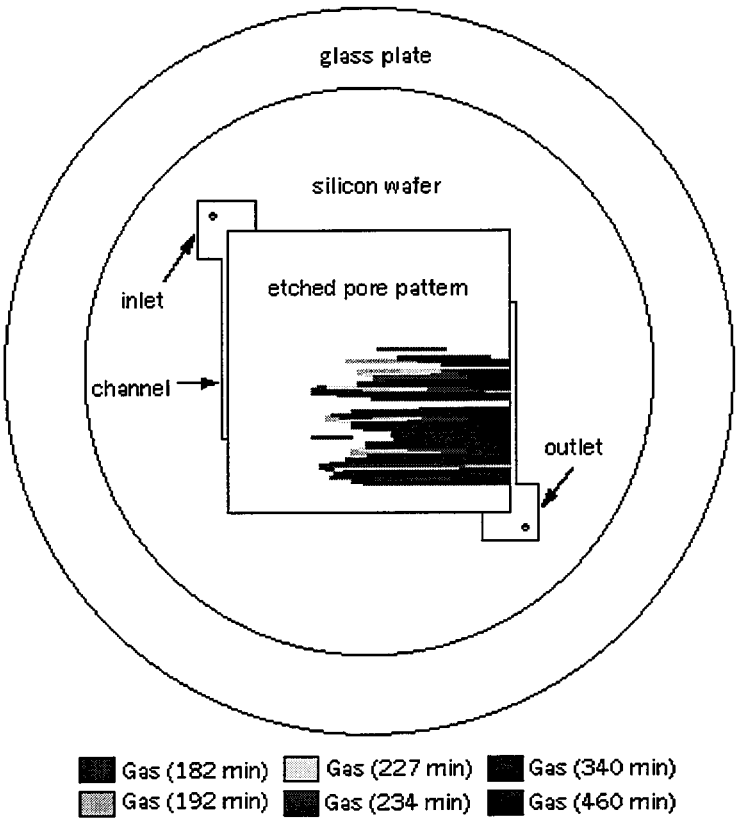


**Figure 3.12: Growth of high gas saturation zones in the micromodel.**

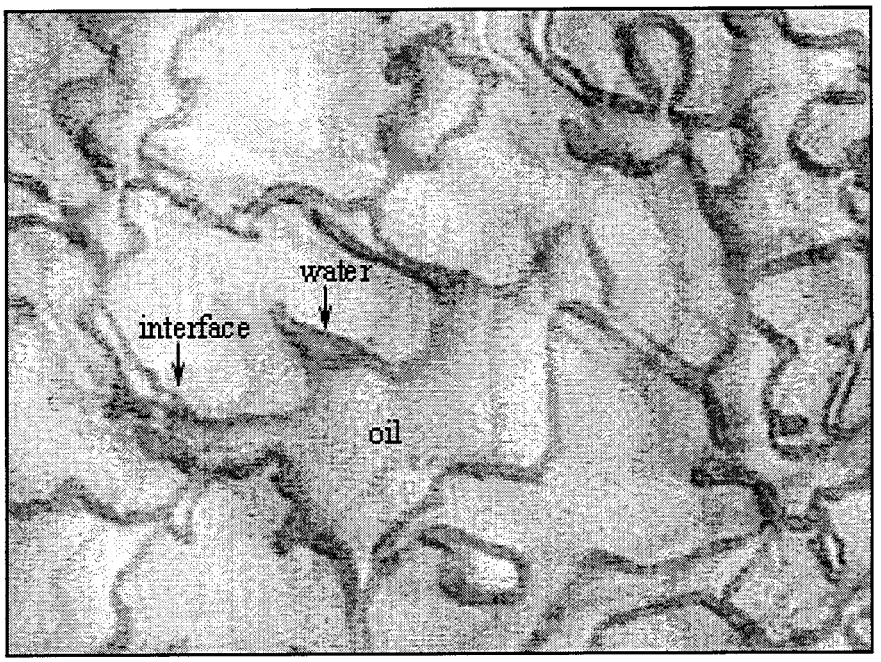


**Figure 3.13a: Gas-oil and water-oil interfaces.**

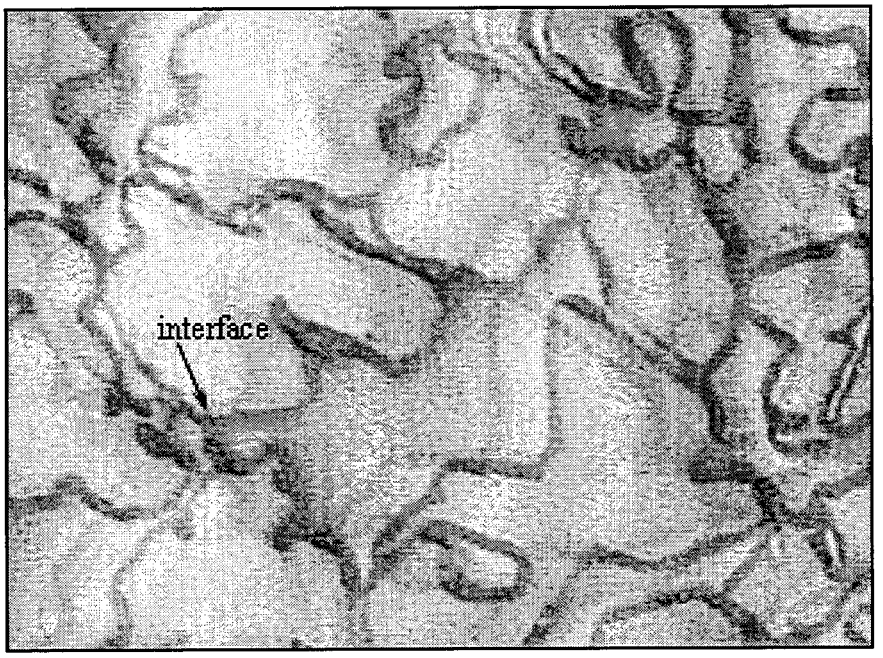


**Figure 3.13b: The gas-oil interface advances toward the pore space.**

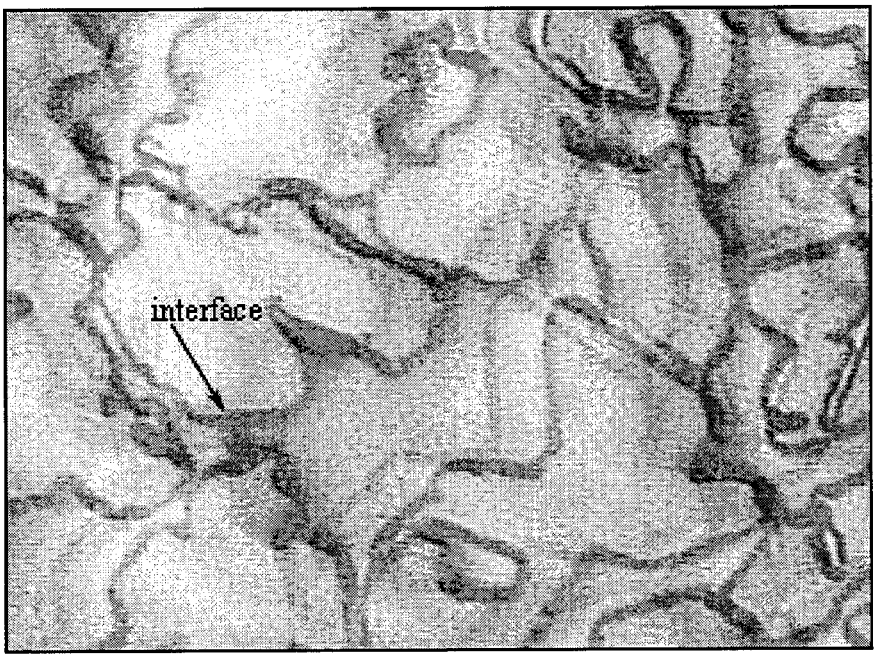


**Figure 3.13c: The interface continues to advance.**

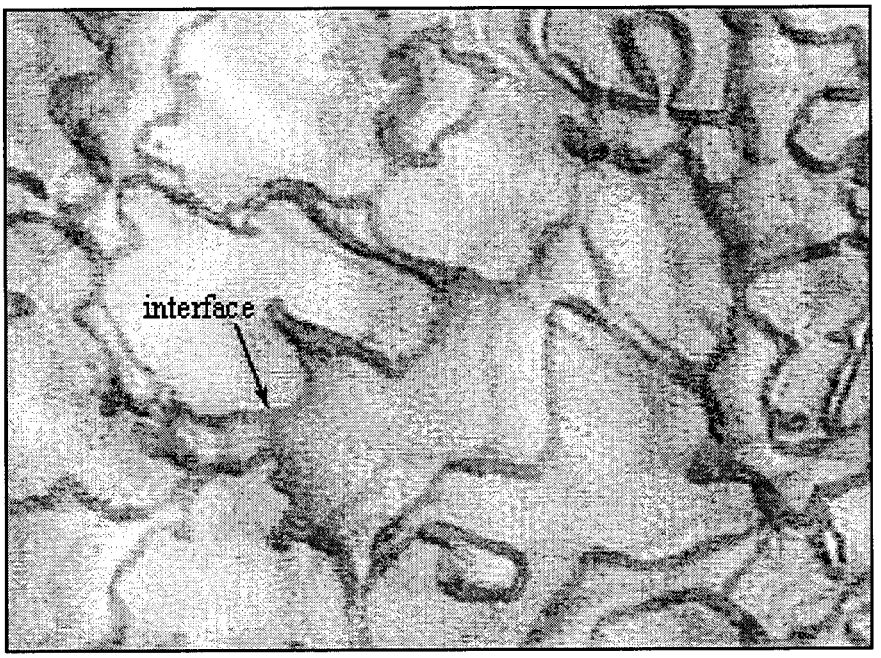


**Figure 3.13d: The interface is at the pore space.**

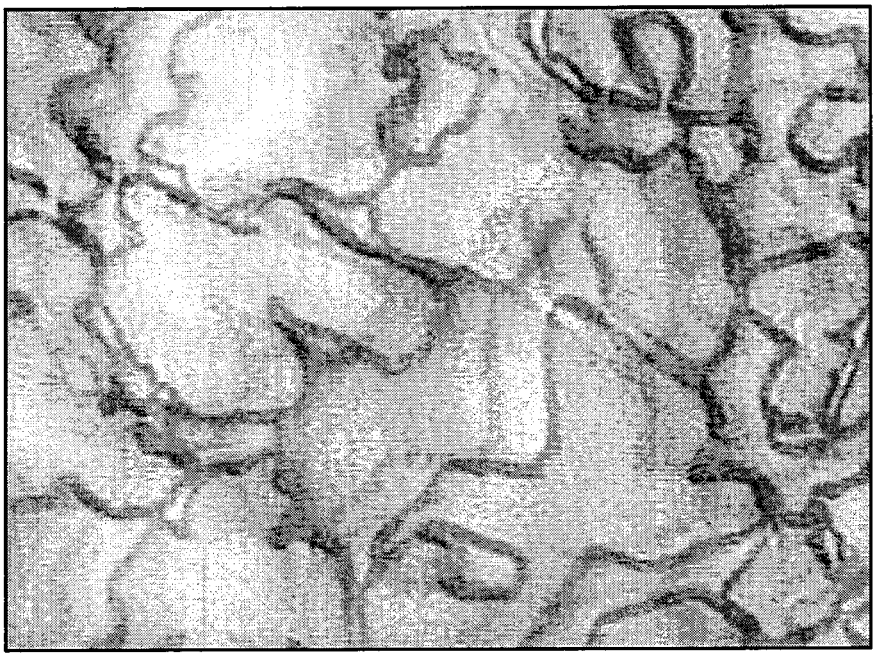

**Figure 3.13e: The gas-oil interface advances to the maximum extent.**

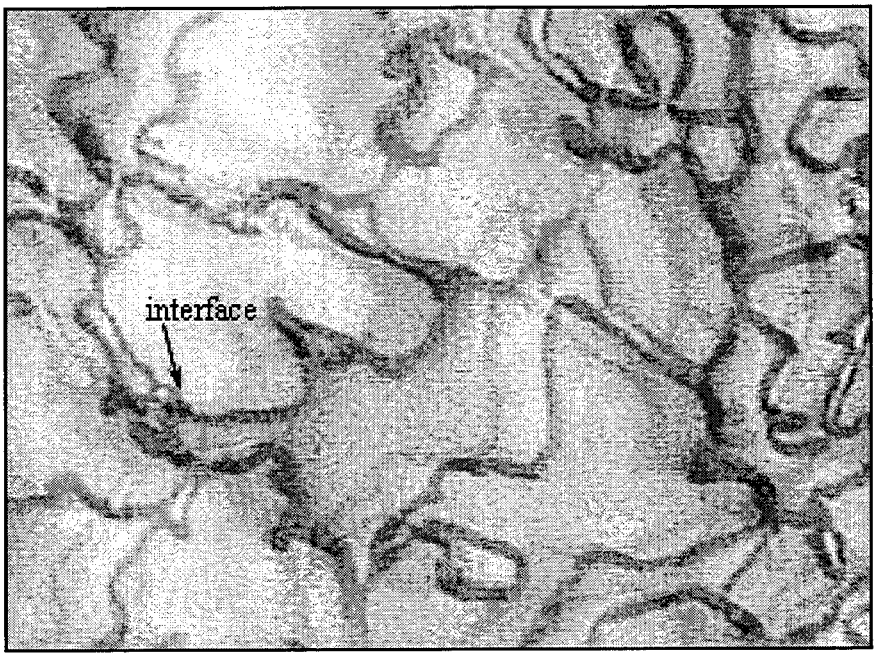


**Figure 3.13f: The gas-oil interface returns to the original location.**

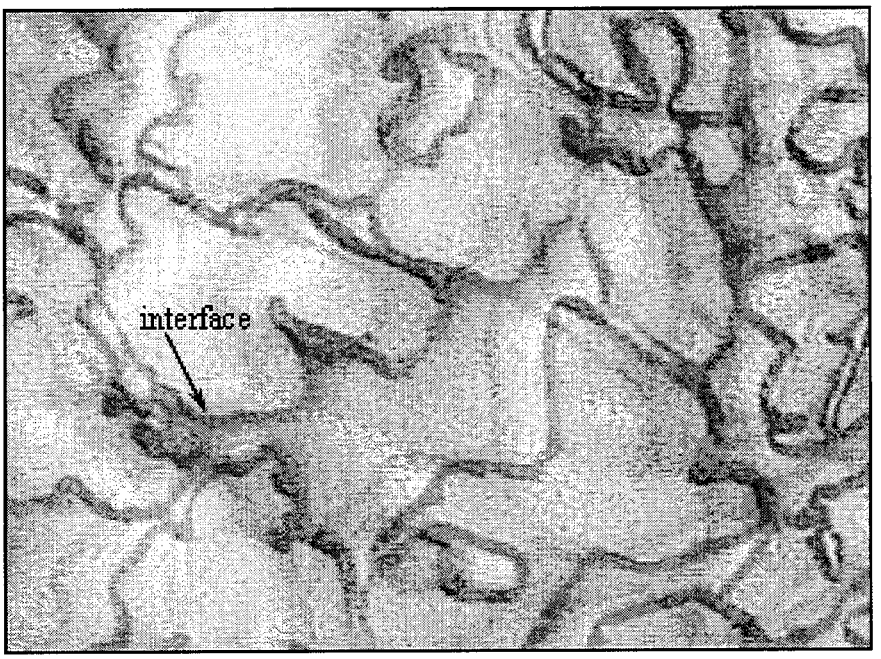


**Figure 3.13g: The gas-oil interface begins to move toward the pore space again.**

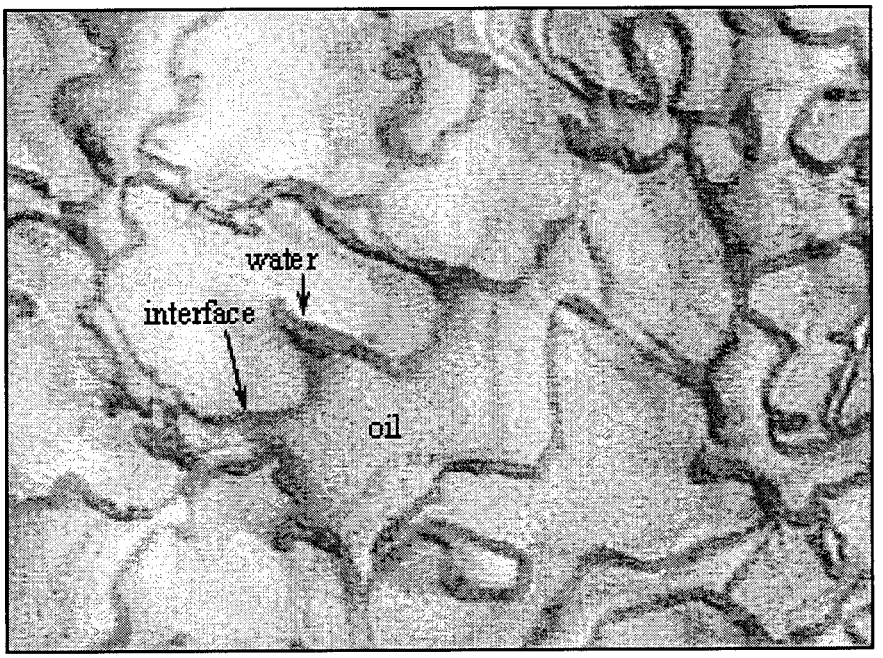


**3.13h: The gas-oil interface continues to move toward the pore space.**

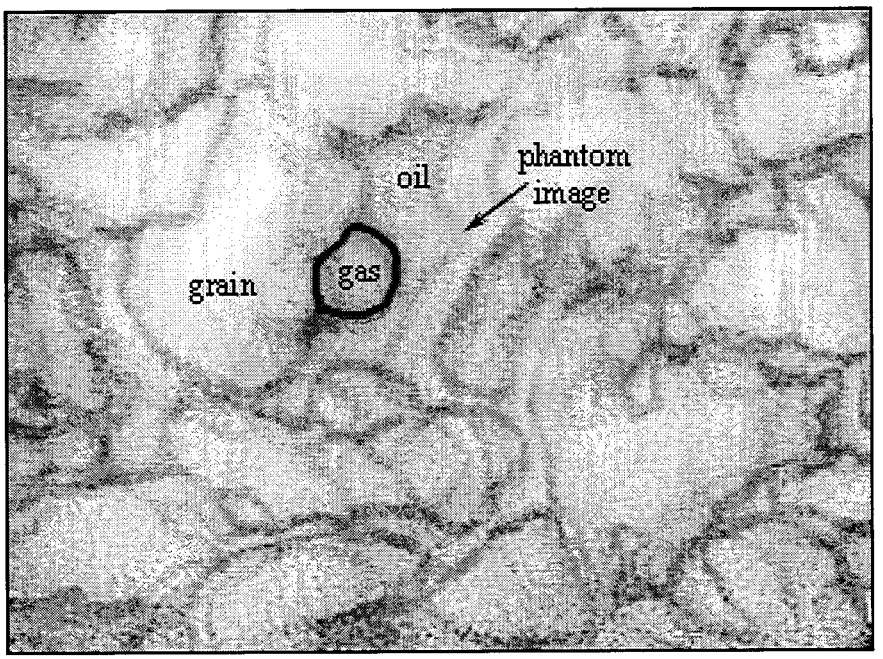


**Figure 3.14a: A recently nucleated gas bubble adheres to a pore wall.**

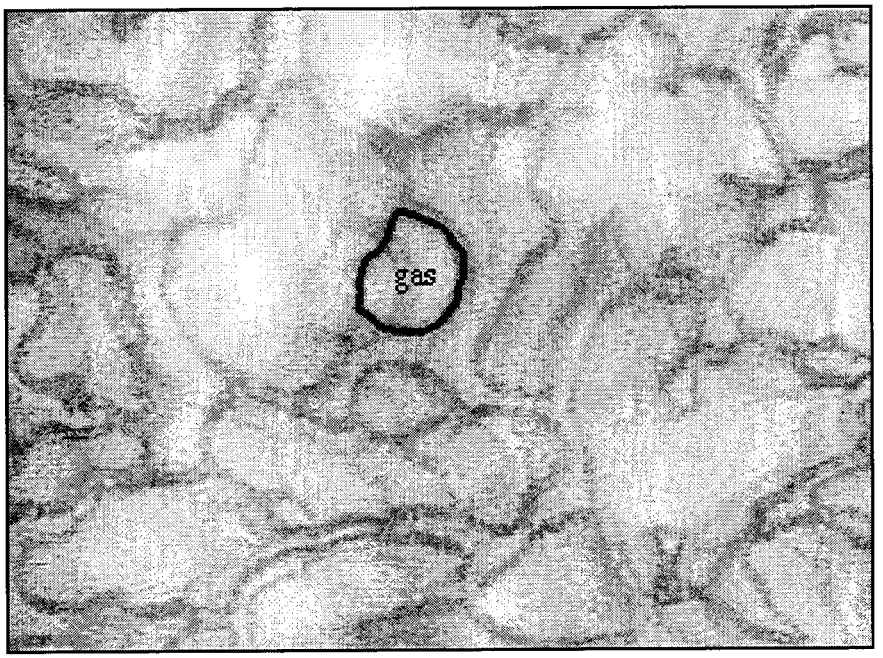


**Figure 3.14b: The gas bubble expands.**

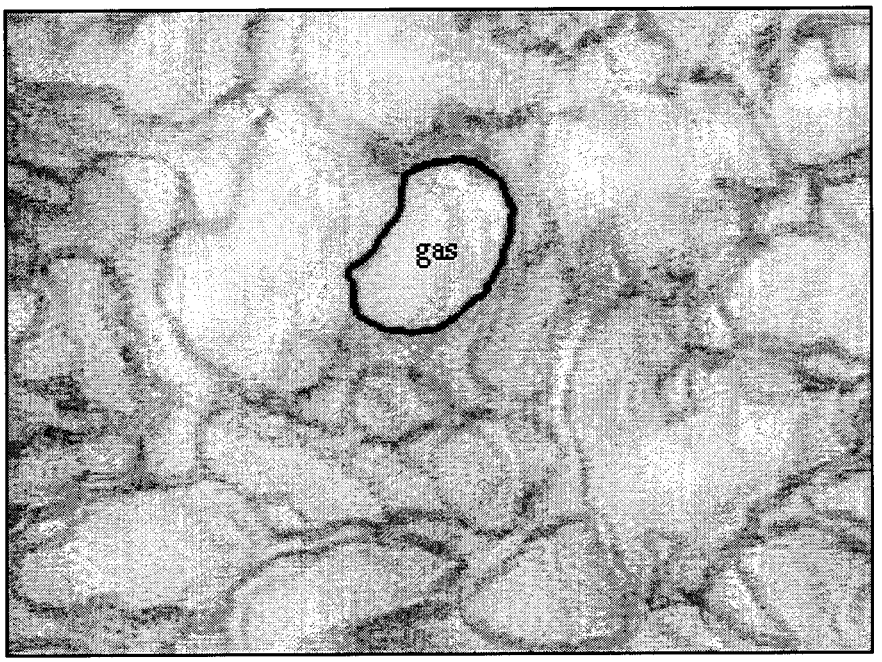


**Figure 3.14c: Expansion continues.**

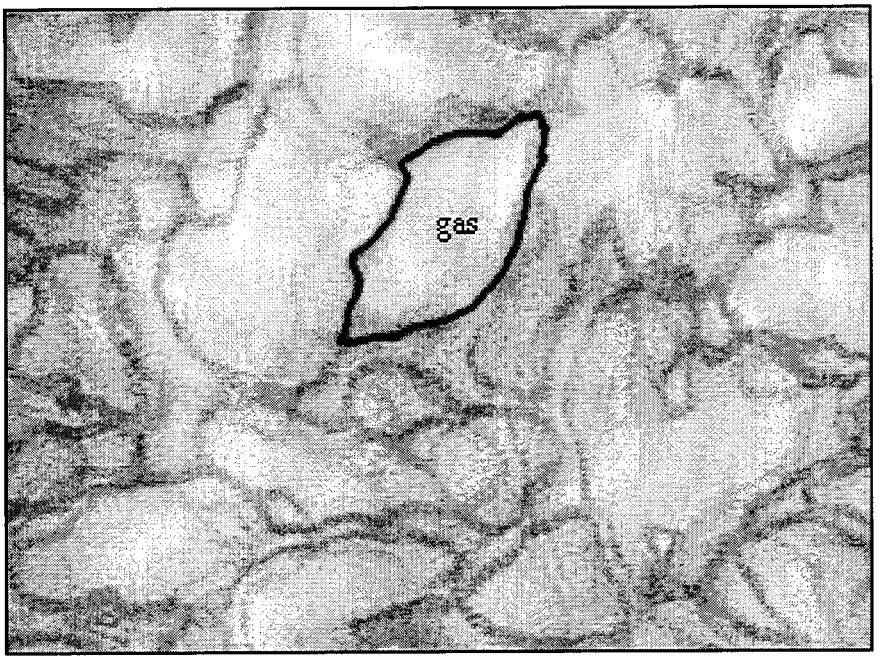


**Figure 3.14d: The gas bubble fills most of the large pore.**

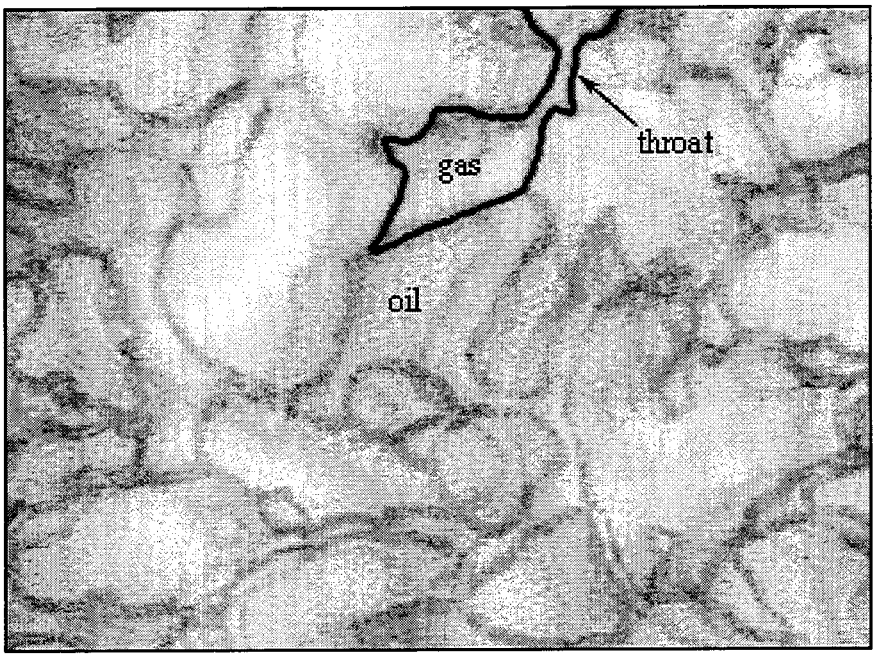


**Figure 3.14e: The gas bubble begins to flow out of the pore.**

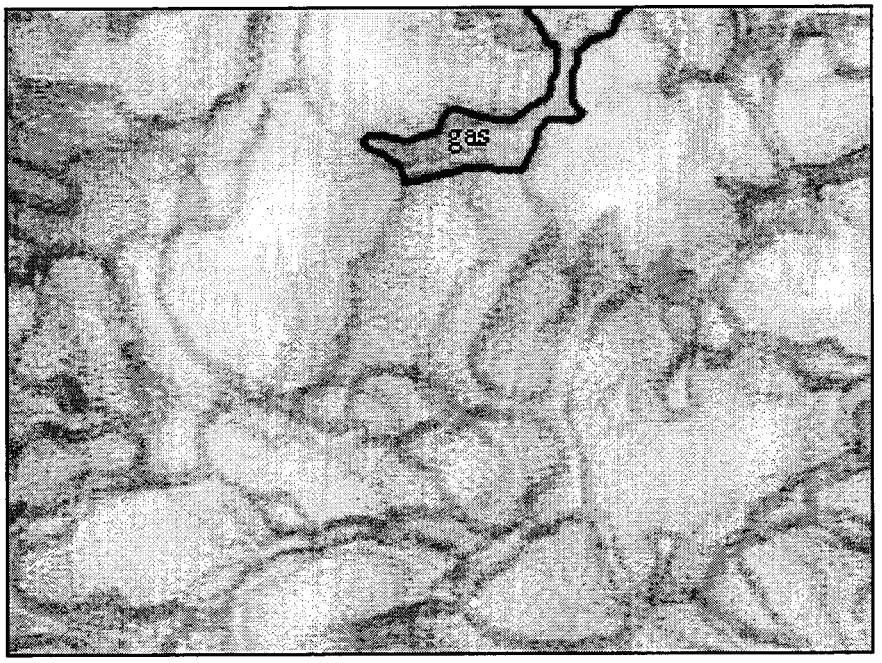


**Figure 3.14f: The gas vacates the pore. There is no visible gas at the nucleation site.**

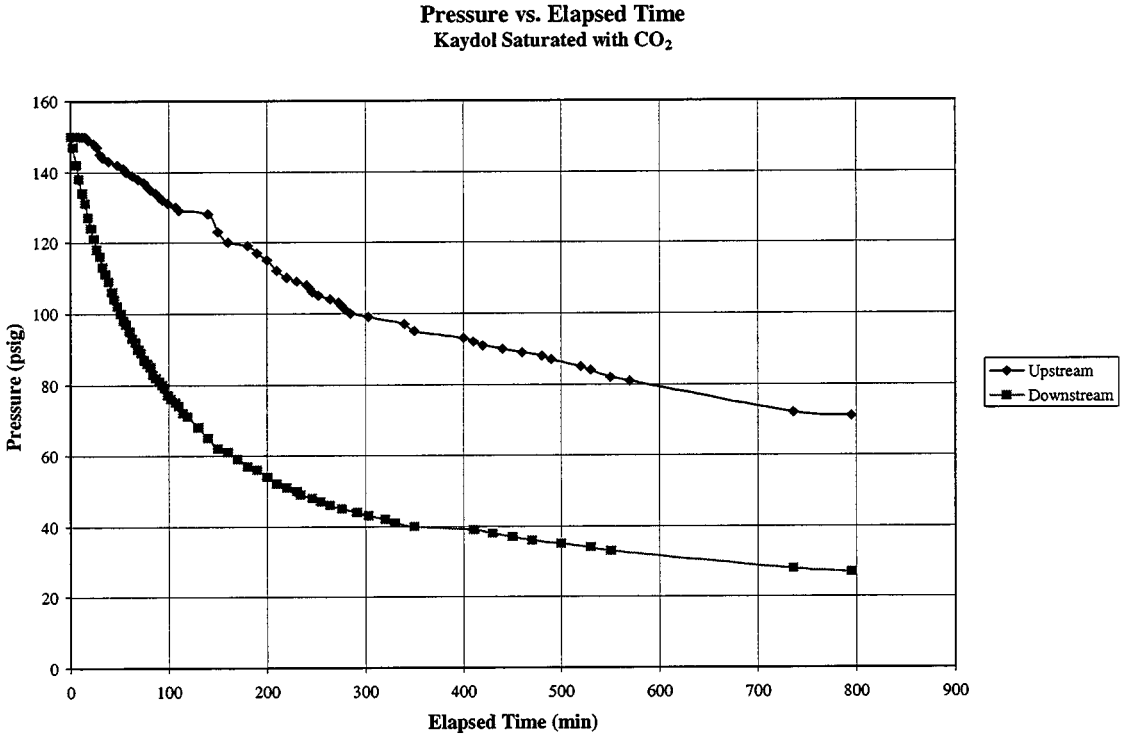


**Figure 3.15: Pressure versus time for Kaydol saturated with $CO_2$ at an unknown pressure.**

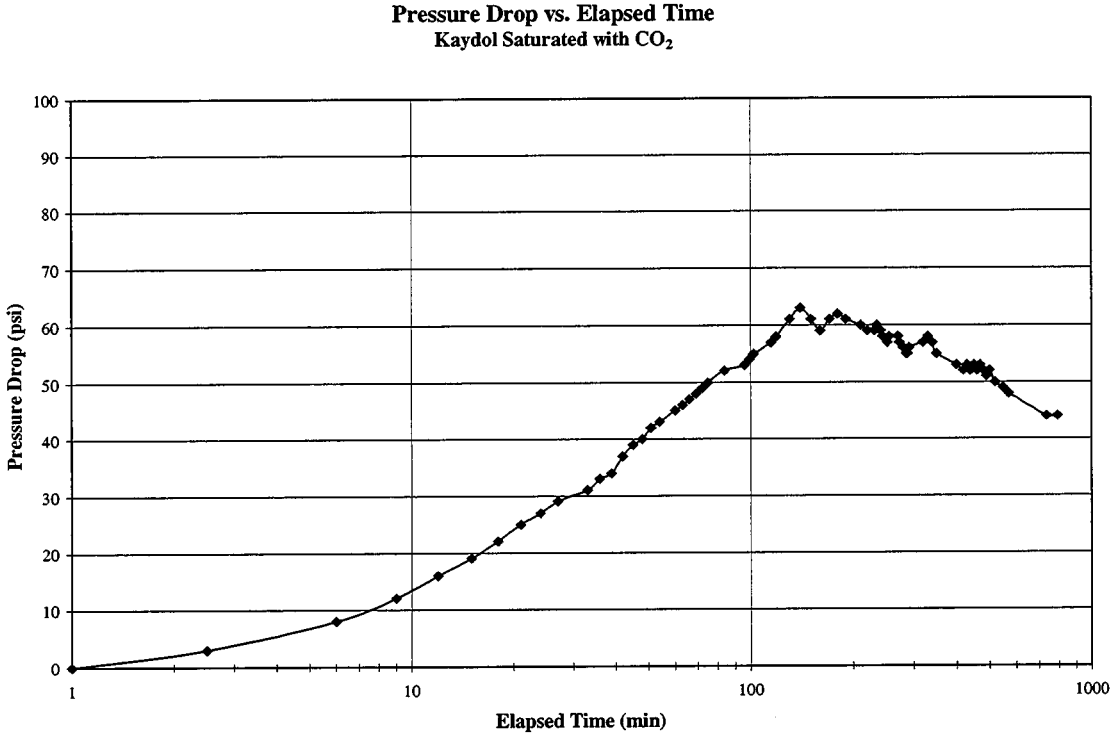


**Figure 3.16: Pressure drop versus time for Kaydol saturated with $CO_2$ at an unknown pressure.**

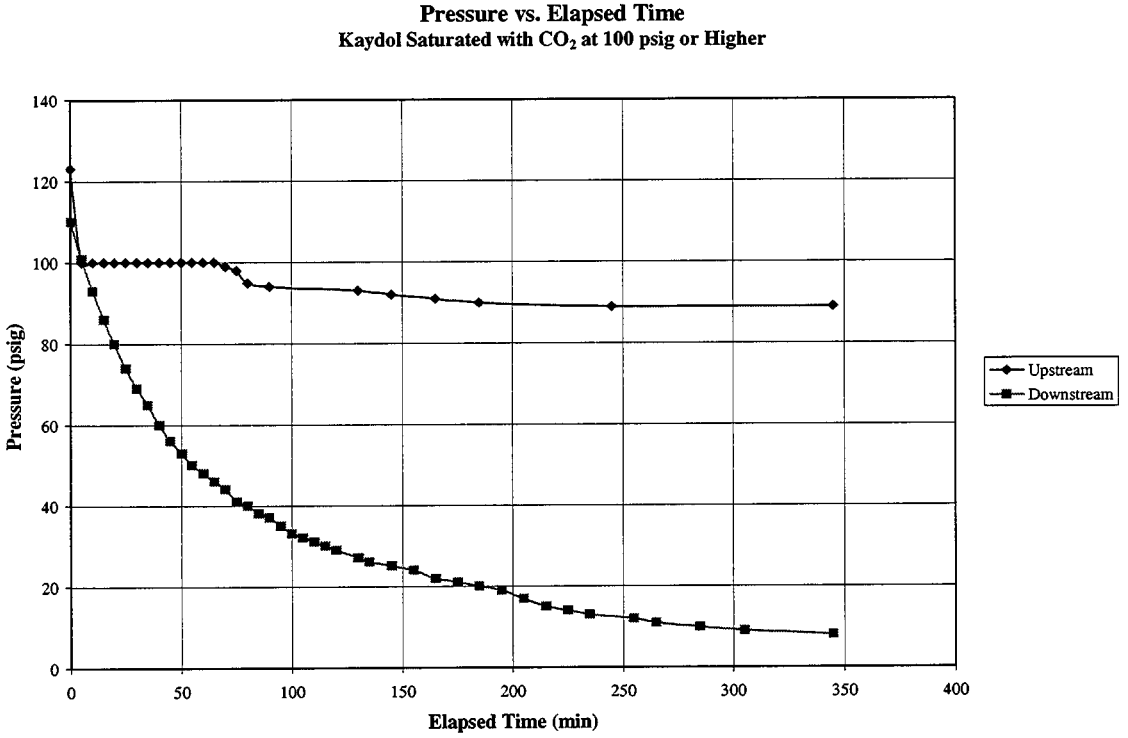


**Figure 3.17: Pressure versus time for Kaydol saturated with $CO_2$ at 100 psig or higher.**

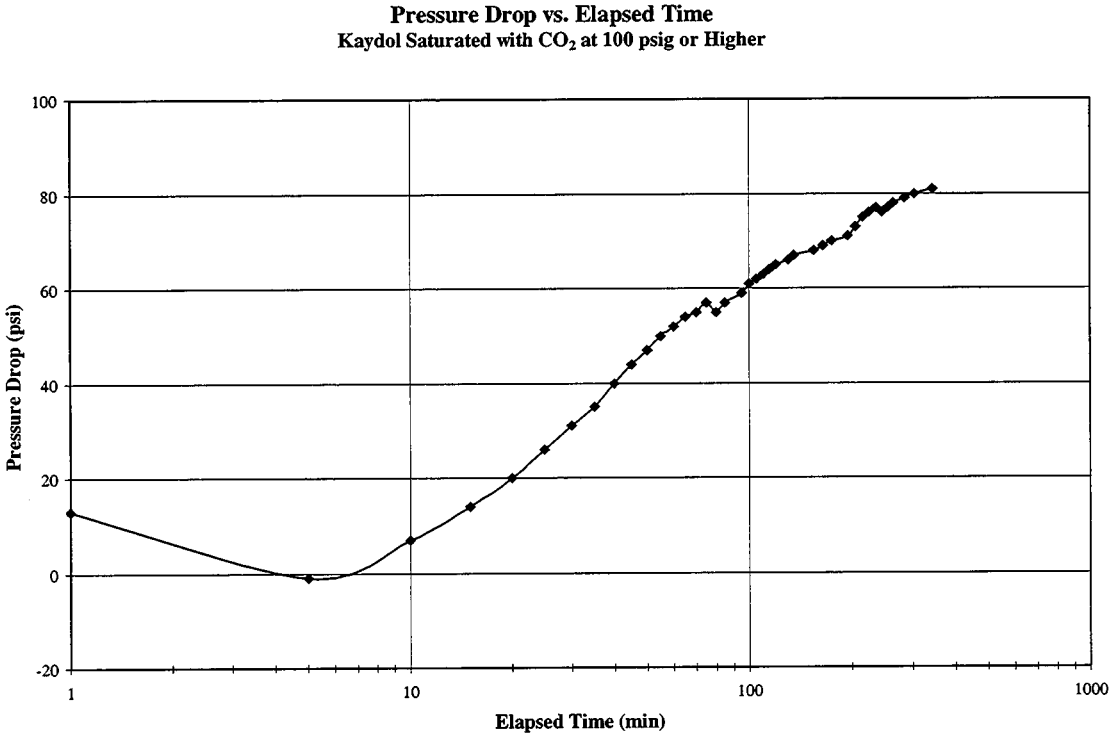


**Figure 3.18: Pressure drop versus time for Kaydol saturated with $CO_2$ at 100 psig or higher.**

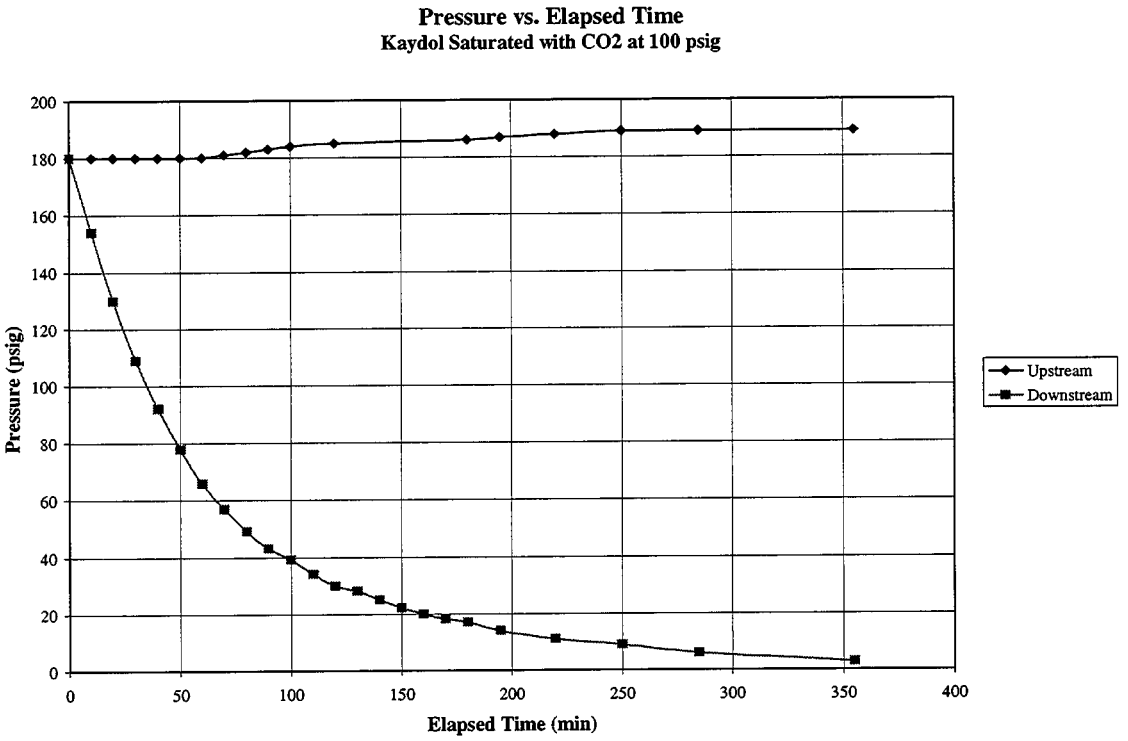


**Figure 3.19: Pressure versus time for Kaydol saturated with $CO_2$ at 100 psig.**

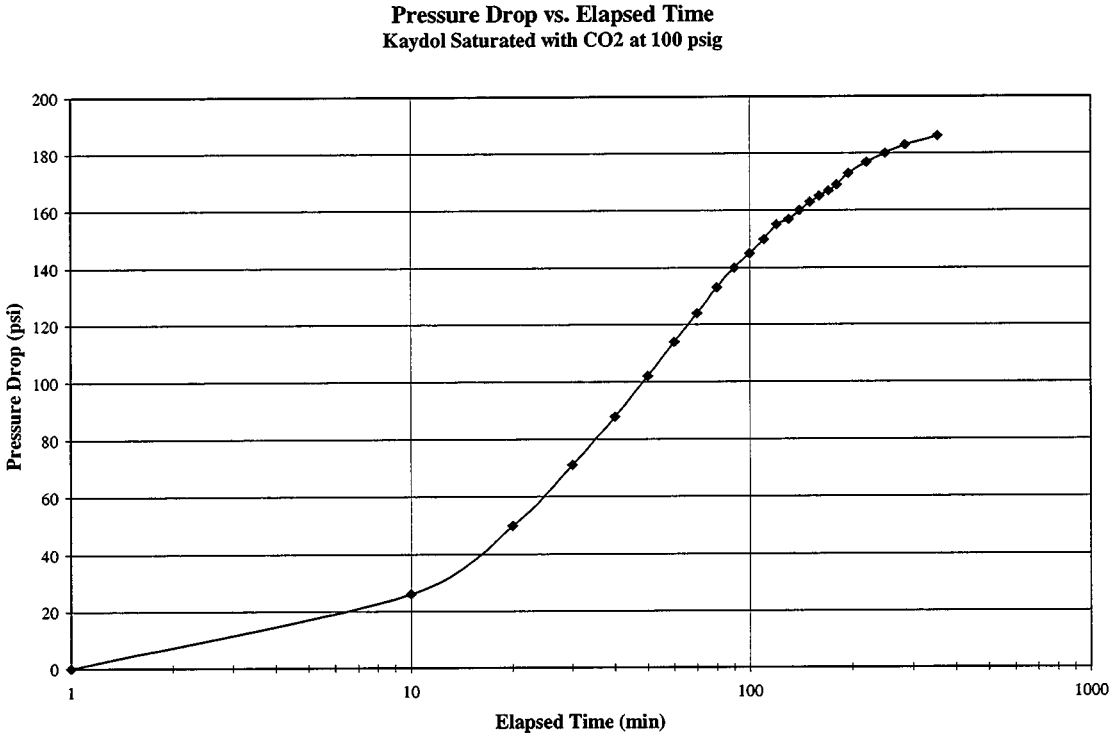


**Figure 3.20: Pressure drop versus time for Kaydol saturated with $CO_2$ at 100 psig.**

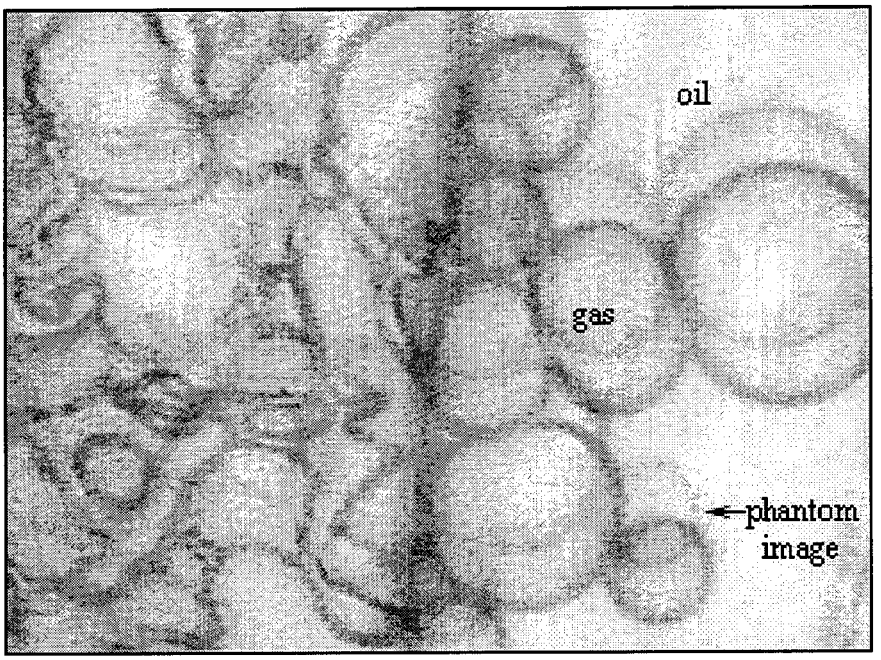


**Figure 3.21: Gas bubbles in the outlet channel. Note deformed interfaces.**

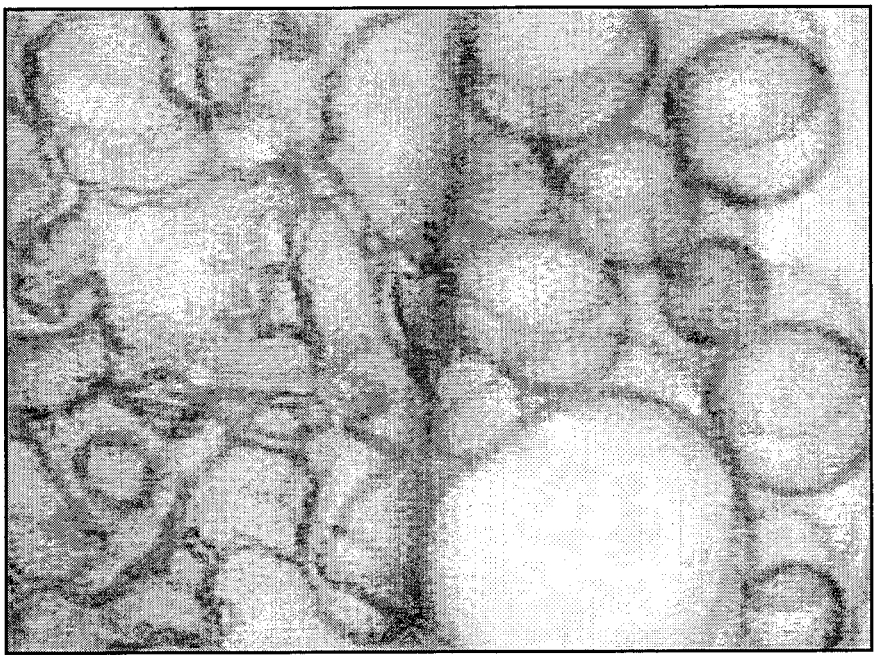

**Figure 3.22: A large bubble with a flattened gas-oil interface.**

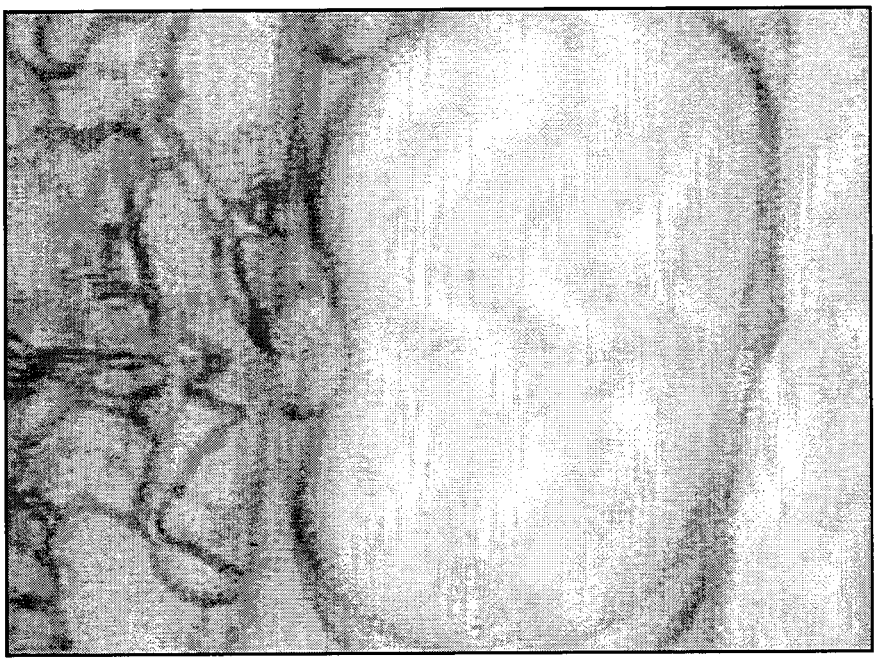

**Figure 3.23: The interface of the large bubble is pressed into a concave shape.**

# 4. CONCLUSIONS

An experimental apparatus has been developed that allows for the observation of pore-scale flow phenomena in micromodels at variable pressures and temperatures. The apparatus was tested and used to perform visual investigations of solution gas drive phenomena. Typical pore-scale flow events, such as liquid-lens breathing, bubble coalescence, and bubble snap-off, were observed.

Gas bubble nucleation was observed repeatedly at a nucleation site during a pressure decline experiment with a water-$CO_2$ system. No pre-existent gas bubble was observed at the nucleation site under 200 X magnification, representing a minimum resolution of 1 μm. A gas bubble was clearly observed to enter solution in the liquid phase at the same nucleation site, where it disappeared from view. Several cases of heterogeneous-type gas dissolution were noted. Homogeneous-type gas dissolution events, in which gas bubbles dissolved into the liquid phase away from any solid surfaces, were commonly observed also. While pore geometry may not have a great effect on gas dissolution, the observations made during this study certainly indicate that pore geometry strongly affects gas nucleation. Few nucleation sites were observed. All of the observed nucleation began at pore walls or at dirt spots. Solid particles were frequently deposited where gas bubbles completely dissolved into the liquid phase. The particles appeared to be attracted to gas-water or gas-oil interfaces, and transported with the interfaces. There was no evidence of instantaneous nucleation. The visual observations seem to indicate that heterogeneous nucleation is the method by which the gas phase forms in porous media.

Liquid viscosity was seen to have an affect on some processes during experimentation. First, for similar volume expansion rates, the recorded pressures and pressure drop in Kaydol-$CO_2$ systems did not change as quickly as in water-$CO_2$ systems. This is due to the relatively high viscosity of Kaydol. The possibility that viscosity could affect the ability of gas bubbles to coalesce was also noted. Gas bubbles coalesce immediately upon contact in water-$CO_2$ systems. In Kaydol-$CO_2$ systems, however, the oil films exhibited much more strength. Coalescence did not usually occur immediately after gas bubbles came into contact. The gas bubbles were even observed to press together with the gas-oil interfaces deformed in the process. Coalescence usually occurred several minutes after contact.

## 5. REFERENCES


1. Abgrall, E. and Iffly, R.: "Etude Physique des Ecoulements par Expansion des Gaz Dissous," *Revue de L'Institut Français du Pétrole* (September-October 1973) 667-692. [As cited by Yortsos and Parlar (1989)].

2. Bora, R., Maini, B.B. and Chakma, A.: "Flow Visualization Studies of Solution Gas Drive Process in Heavy Oil Reservoirs Using a Glass Micromodel," Paper SPE 37519 presented at the 1997 SPE International Thermal Operations and Heavy Oil Symposium, Bakersfield, CA (10-12 February 1997).

3. Campbell, B.T. and Orr Jr., F.M.: "Flow Visualization for $CO_2$/Crude-Oil Displacements," *SPEJ* (October 1985) 665-678.

4. Castanier, L.M. and Sagar, N.S.: "Pore Level Visualization of Oil-Foam Interactions in a Silicon Micromodel," Paper SPE 39512 presented at the SPE India and Gas Conference and Exhibition, New Delhi, India (7-9 April 1998).

5. Chatenever, A., Indra, M.K. and Kyte, J.R.: "Microscopic Observations of Solution Gas Drive Behavior," *JPT* (June 1959) 13-15.

6. Coşkuner, G.: "Microvisual Study of Multiphase Gas Condensate Flow in Porous Media," *Transport in Porous Media* **28** (1997) 1-18.

7. Danesh, A., Peden, J.M., Krinis, D. and Henderson, G.D.: "Pore Level Visual Investigation of Oil Recovery by Solution Gas Drive and Gas Injection," Paper SPE 16956 presented at the 62$^{nd}$ Annual Technical Conference and Exhibition of the SPE, Dallas, TX (27-30 September 1987).

8. Davis Jr., J.A. and Jones, S.C.: "Displacement Mechanisms of Micellar Solutions," *JPT* (December 1968) 1415-1428.

9. Dumore, J.M.: "Development of Gas Saturations During Solution-Gas Drive in an Oil Layer Below a Gas Cap," *SPEJ* (September 1970) 211-218.

10. El-Yousfi, A., Zarcone, C., Bories, S. and Lenormand, R.: "Physical Mechanisms for Bubble Growth during Solution Gas Drive," Paper SPE 38921 presented at the 72$^{nd}$ Annual Technical Conference and Exhibition of the SPE, Dallas, TX (5-8 October 1997).

11. Firoozabadi, A., Ottesen, B. and Mikkelsen, M.: "Measurements of Supersaturation and Critical Gas Saturation," *SPE Formation Evaluation* (December 1992) 337-344.

12. Firoozabadi, A. and Kashchiev, D.: "Pressure and Volume Evolution During Gas Phase Formation in Solution Gas Drive Process," *SPEJ* (September 1996) 219-227.

13. Firoozabadi, A.: "Author's Reply to Discussion of Pressure and Volume Evolution During Gas Phase Formation in Solution Gas Drive Process," *SPEJ* (June 1997) 228-231.

14. Handy, L.L.: "A Laboratory Study of Oil Recovery by Solution Gas Drive," *Petr. Trans. AIME*, **213** (1958) 310-315.

15. Hornbrook, J.W., Castanier, L.M. and Petit, P.A.: "Observation of Foam/Oil Interactions in a New, High-Resolution Micromodel," Paper SPE 22631 presented at the 66th Annual Technical Conference and Exhibition of the SPE, Dallas, TX (6-9 October 1991).

16. Hunt Jr., E.B. and Berry Jr., V.J.: "Evolution of Gas from Liquids Flowing Through Porous Media," *AIChE*, **2** (1956) 560-567.

17. Kennedy, H.T. and Olson, R.: "Bubble Formation in Supersaturated Hydrocarbon Mixtures," *Petr. Trans. AIME*, **195** (1952) 271-278.

18. Kortekaas, T.F.M. and van Poelgeest, F.: "Liberation of Solution Gas During Pressure Depletion of Virgin and Watered-Out Oil Reservoirs," *SPERE* (August 1991) 329-335.

19. Kuhlman, M.I.: "Visualizing the Effect of Light Oil on $CO_2$ Foams," *JPT* (July 1990) 902-908.

20. Li, X., and Yortsos, Y.C.: "Visualization and Numerical Studies of Bubble Growth during Pressure Depletion," Paper SPE 22589 presented at the 66th Annual Technical Conference and Exhibition of the SPE, Dallas, TX (6-9 October 1991).

21. Li, X., and Yortsos, Y.C.: "Critical Gas Saturation: Modeling and Sensitivity Studies," Paper SPE 26662 presented at the 68th Annual Technical Conference and Exhibition of the SPE, Houston, TX (3-6 October 1993).

22. Li, X. and Yortsos, Y.C.: "Bubble Growth and Stability in an Effective Porous Medium," *Phys. Fluids A*, **6** (5) (May 1994) 1663-1676.

23. Li, X. and Yortsos, Y.C.: "Visualization and Simulation of Bubble Growth in Pore Networks," *AIChE* (February 1995) 214-222.

24. Li, X. and Yortsos, Y.C.: "Theory of Multiple Bubble Growth in Porous Media by Solute Diffusion," *Chem. Eng. Sci.*, **50** (8) (1995).

25. Mackay, E.J., Henderson, G.D., Tehrani, D.H. and Danesh, A.: "The Importance of Interfacial Tension on Fluid Distribution During Depressurization," *SPERE*, (October 1998) 408-415.

26. Madaoui, K.: "Conditions de Mobilité de la Phase Gazeuse lors de la Décompression d'un Mélange d'Hydrocarbures en Milieu Poreux," Thesis, Toulouse U., France (1975). [As cited by Firoozabadi, *et. al.* (1992)].

27. Mattax, C.C. and Kyte, J.R.: "Ever See a Water Flood?," *Oil and Gas J.* (16 October 1961) 115-128.

28. Moulu, J.C. and Longeron, D.L.: "Solution-Gas Drive: Experiments and Simulation," *Proc.*, 5th European Symposium on Improved Oil Recovery, Budapest (1989). [As cited by Firoozabadi, *et. al.* (1992)].

29. Owete, O.S. and Brigham, W.E.: "Flow Behavior of Foam: A Porous Micromodel Study," *SPERE* (August 1987) 315-323.

30. Peden, J.M. and Husain, M.I.: "Visual Investigation of Multiphase Flow and Phase Interactions Within Porous Media," Paper SPE 14307 presented at the 60th Annual Technical Conference and Exhibition of the SPE, Las Vegas, NV (22-25 September 1985).

31. Satik, C., Li, X. and Yortsos, Y.C.: "Scaling of Single-Bubble Growth in a Porous Medium," *Phys. Rev. E*, **51** (4) (April 1995) 3286-3295.

32. Stewart, C.R., Craig, F.F. and Morse, R.A.: "Determination of Limestone Performance Characteristics by Model Flow Tests," *Petr. Trans. AIME*, **198** (1953) 93-102.

33. Stewart, C.R., Hunt Jr., E.B., Geffen, T.M. and Berry Jr., V.J.: "The Role of Bubble Formation in Oil Recovery by Solution Gas Drive in Limestones," *Petr. Trans. AIME*, **201** (1956) 560-567.

34. Wall, C.G. and Khurana, A.K.: "Saturation: Permeability Relationships at Low Gas Saturations," *J. Inst. Pet.*, **57** (September 1971) 261-269.

35. Wall, C.G. and Khurana, A.K.: "The Effect of Rate Pressure Decline and Liquid Viscosity on Low-Pressure Gas Saturations in Porous Media," *J. Inst. Pet.*, **58** (November 1972) 335-345.

36. Wieland, D.R. and Kennedy, H.T.: "Measurement of Bubble Frequency in Cores," *Petr. Trans. AIME*, **210** (1957) 122-125.

37. Wood Jr., J.W.: "Bubble Formation in Rangely Field, Colorado," MS Thesis, Texas A&M U., College Station (1953). [As cited by Firoozabadi, *et. al.* (1992)].

38. Yortsos, Y.C. and Parlar, M.: "Phase Change in Binary Systems in Porous Media: Application to Solution Gas Drive," Paper SPE 19697 presented at the 64th Annual Technical Conference and Exhibition of the SPE, San Antonio, TX (8-11 October 1989).

39. Yortsos, Y.C.: "Discussion of Pressure and Volume Evolution During Gas Phase Formation in Solution Gas Drive Processes," *SPEJ* (June 1997) 223-227.